

A revised and expanded deep radiostratigraphy of the Greenland Ice Sheet from airborne radar sounding surveys between 1993–2019

Joseph A. MacGregor¹, Mark A. Fahnestock², John D. Paden³, Jilu Li³, Jeremy P. Harbeck⁴, Andy Aschwanden²

¹ Cryospheric Sciences Laboratory, NASA Goddard Space Flight Center, Greenbelt, Maryland, United States of America

² Geophysical Institute, University of Alaska Fairbanks, Fairbanks, Alaska, United States of America

³ Center for Remote Sensing and Integrated Systems, The University of Kansas, Lawrence, Kansas, United States of America

⁴ ADNET Systems, Bethesda, Maryland, United States of America

Correspondence to: Joseph A. MacGregor (joseph.a.macgregor@nasa.gov)

Abstract. Between 1993 and 2019, NASA and NSF sponsored 26 separate airborne campaigns that surveyed the thickness and radiostratigraphy of the Greenland Ice Sheet using successive generations of coherent VHF radar sounders developed and operated by The University of Kansas. Most of the ice-sheet’s internal VHF radiostratigraphy is composed of isochronal reflections that record its integrated response to past centennial-to-multi-millennial-scale climatic and dynamic events. We previously generated the first comprehensive dated radiostratigraphy of the Greenland Ice Sheet using the first 20 of these campaigns (1993–2013) and investigated its value for constraining the ice sheet’s history and modern boundary conditions. Here we describe the second version of this radiostratigraphic dataset using all 26 campaigns, which includes substantial improvements in survey coverage and was mostly acquired with higher-fidelity systems. We improved quality control and accelerated reflection tracing and matching by including an automatic test for stratigraphic conformability, a thickness-normalized reprojection for radargrams, and automatic inter-segment reflection matching. We reviewed and augmented the 1993–2013 radiostratigraphy, and we applied an existing independently developed method for predicting radiostratigraphy to the previously untraced campaigns (2014–2019) to accelerate their semi-automatic tracing. The result is a more robust radiostratigraphy and age structure of the ice sheet that covers up to 65% of the ice sheet and includes >58 600 km of newly traced reflections from the 2014–2019 campaigns. This dataset can be used to validate the sensitivity of ice-sheet models to past major climate changes and constrain long-term boundary conditions (e.g., accumulation rate). Based on these results, we make several recommendations for how radiostratigraphy may be traced more efficiently and reliably in the future. This dataset is freely available at <https://doi.org/10.5281/zenodo.15132763> (MacGregor et al., 2025). It includes all traced reflections at the spatial resolution of the radargrams and grids (5 km horizontal resolution) of the depths of isochrones between 3–115 ka and ages between 10–80% of the ice thickness; associated codes are available at <https://doi.org/10.5281/zenodo.14183061> (MacGregor, 2024a).

30 1 Introduction

31 The Greenland Ice Sheet (*GrIS*) is losing mass rapidly and is projected to do so for the foreseeable future unless substantial
32 mitigation of anthropogenic warming is undertaken (Aschwanden et al., 2019; Goelzer et al., 2020; Otsuka et al., 2023). Ice-
33 sheet models are the essential tools used to make these projections, but the uncertainty in these projections is large and
34 significantly affects how society might respond to the global and regional sea-level change caused by GrIS wastage
35 (Aschwanden et al., 2021). Numerous efforts are underway to reduce this uncertainty (e.g., Aschwanden and Brinkerhoff,
36 2022), and among the major challenges that these efforts seek to address are the initialization of these models prior to applying
37 projected external forcings (typically atmospheric and oceanic) and whether their long-term sensitivity to anthropogenic
38 climate change is consistent with that inferred from paleoclimatic records (e.g., Goelzer et al., 2018; Briner et al., 2020).
39 Fortunately, the GrIS contains within itself a substantial and spatially well-distributed archive of its integrated response to past
40 climate change: its isochronal radiostratigraphy. Further, this radiostratigraphy can constrain the subsurface state and dynamics
41 of the present-day GrIS in a manner not achieved by other spatially distributed observations; it is also potentially valuable for
42 identifying well-initialized instances of ice-sheet models (e.g., Bingham et al., in review).

43 MacGregor et al. (2015a) (hereafter *M15*) generated the first large-scale dated radiostratigraphy of the GrIS. That study
44 was made possible by the abundance of high-quality very high frequency (*VHF*) airborne-radar sounding data collected in the
45 prior two decades (1993–2013, all years CE) sponsored by the United States’ (*US*) National Aeronautics and Space
46 Administration (*NASA*) and National Science Foundation (*NSF*; *CRISIS*, 2024), advances in radar-sounder design led by The
47 University of Kansas (*KU*; e.g., Gogineni et al., 1998) and its Center for Remote Sensing and Integrated Systems (*CRISIS*;
48 e.g., Rodríguez-Morales et al., 2014; Arnold et al., 2020), and a suite of synchronized deep ice cores collected by international
49 consortiums led primarily by Denmark and the United States (e.g., Rasmussen et al., 2006; Dahl-Jensen et al., 2013; Seierstad
50 et al., 2014; Mojtabavi et al., 2020). *M15* introduced several advances in prediction, mapping, dating, validation and gridding
51 of radiostratigraphy to generate the first ice-sheet-wide age volume for either of Earth’s two remaining ice sheets. That study
52 enabled numerous improvements in mapping of key ice-sheet boundary conditions (e.g., MacGregor et al., 2015b, 2016a,b,
53 2022; Dow et al., 2018). It also motivated refinements to – and assessment of – methods for mapping and modeling
54 radiostratigraphy (e.g., Born, 2017; Xiong et al., 2018; Delf et al., 2020; Born and Robinson, 2021). However, no subsequent
55 study has significantly improved upon the *M15* dataset itself, either by infilling isochronal reflections that were unmapped by
56 *M15* or by incorporating the large quantity of additional similar airborne-radar sounding data collected as part of *NASA*’s
57 Operation IceBridge (*OIB*) in 2014–2019 that was not included in *M15* (MacGregor et al., 2021).

58 Here we describe version 2 (*v2*) of the GrIS radiostratigraphy dataset and the methods to generate it, with a particular
59 emphasis on methodological improvements introduced since *M15* and remaining uncertainties. Based on the development of
60 this dataset, we identify future opportunities for developing a more complete deep radiostratigraphy of the GrIS and make
61 recommendations for future improvements in tracing methods.

62 2 Airborne radar-sounding data

63 To build this second version of the GrIS-wide radiostratigraphy, we first evaluate the same 1993–2013 VHF radar-sounding
 64 data collected over the GrIS by KU/CReSIS as M15 used to generate v1 (Table 1; Fig. 1; CReSIS, 2024). We further consider
 65 the additional six OIB campaigns worth of VHF radar-sounding data collected annually during boreal springtime between
 66 2014–2019 by KU/CReSIS using identical or similar system configurations. These data were recorded coherently and
 67 subsequently focused using synthetic aperture radar (*SAR*) methods by KU/CReSIS. The nominal vertical resolution of these
 68 processed data is 2.5–4.4 m, which is sufficiently fine to resolve many (often dozens) distinct internal reflections, while their
 69 along-track resolution is more variable (~15–150 m depending on system and campaign). Depending on system performance,
 70 in-flight acquisition decisions and post-processing requirements, individual survey flights are composed of one or more
 71 *segments*, which can be tens to thousands of kilometers long depending on how many segments constitute each flight. Each
 72 segment is further divided into a sequence of ~50-km-long data *frames*, which are the format in which the data are distributed
 73 by KU/CReSIS. For example, the flight on 2011-05-02 (*20110502* in KU/CReSIS nomenclature), is divided into two segments,
 74 (*20110502_01* and *20110502_02*, respectively), which are composed of 38 and 35 frames, respectively (*20110502_01_001–*
 75 *20110502_01_038*, and *20110502_02_001–20110502_02_035*). We evaluate these SAR-focused data “as-is” and do not
 76 perform any substantive re-processing thereof, although we note that at least one focusing method has since been introduced
 77 that is intended to optimize detection of specular internal reflections (Castelletti et al., 2019).

78

79 **Table 1:** NASA/NSF/KU/CReSIS airborne radar sounding surveys of the GrIS between 1993–2019 considered in this study.

| Year | Aircraft type ^a | Radar sounder ^b | Priority rating ^c | Total length evaluated ^d | | Length traced ^e | | | | |
|------|----------------------------|----------------------------|------------------------------|-------------------------------------|-------------------------|----------------------------|-----------|------------|-----------|----------------------|
| | | | | v1 (M15) (km) | v2 (this study) (km) | v1 (km) | v1 (%) | v2 (km) | v2 (%) | v2–v1 change (km) |
| 1993 | P-3B | ICORDS | Low | 17 205 | 1 703 | 4 243 | 25 | 868 | 51 | –3 375 |
| 1995 | P-3B | ICORDS | Low | 13 641 | 4 053 | 6 640 | 49 | 3 853 | 95 | –2 787 |
| 1996 | P-3B | ICORDS | Low | 4 527 | 249 | 2 999 | 66 | 249 | 100 | –2 750 |
| 1997 | P-3B | ICORDS | Medium | 14 123 | 5 885 | 5 922 | 42 | 4 019 | 68 | –1 903 |
| 1998 | P-3B | ICORDS v2 | Medium | 25 977 | 7 052 | 11 538 | 44 | 3 993 | 57 | –7 545 |
| 1999 | P-3B | ICORDS v2 | Medium | 33 993 | 26 493 | 24 409 | 72 | 20 458 | 77 | –3 951 |
| 2001 | P-3B | ICORDS v2 | Medium | 10 899 | 4 530 | 2 623 | 24 | 2 880 | 64 | +257 |
| 2002 | P-3B | ICORDS v2 | Medium | 21 187 | 9 137 | 10 642 | 50 | 7 100 | 78 | –3 542 |
| 2003 | P-3B | ACORDS | Medium | 13 988 | 7 950 | 6 022 | 43 | 4 865 | 61 | –1 157 |
| 2005 | DHC-6 | ACORDS | Low | 6 096 | 0 | 761 | 12 | 0 | 0 | –761 |
| 2006 | DHC-6 | MCRDS | Low | 12 289 | 268 | 1 796 | 15 | 122 | 46 | –1 674 |
| 2007 | P-3B | MCRDS | Medium | 11 846 | 4 303 | 2 192 | 19 | 1 791 | 42 | –401 |

| | | | | | | | | | | |
|-------|--------|-----------|--------|----------------------|---------|---------|-----|---------|-----|---------|
| 2008 | DHC-6 | MCRDS | Low | 22 706 | 8 802 | 7 438 | 33 | 6 526 | 74 | -912 |
| 2009 | DHC-6 | MCRDS | Low | 9 250 | 366 | 341 | 4 | 323 | 88 | -18 |
| 2010 | DC-8 | MCoRDS | Medium | 25 186 | 10 370 | 3 677 | 15 | 3 543 | 34 | -111 |
| 2010 | P-3B | MCoRDS | Medium | 28 171 | 2 547 | 2 840 | 10 | 1 027 | 40 | -1 813 |
| 2011 | P-3B | MCoRDS v2 | High | 74 875 | 31 192 | 25 814 | 34 | 20 987 | 67 | -5 727 |
| 2011 | DHC-6 | MCRDS | Low | 7 172 | 708 | 660 | 9 | 328 | 46 | -332 |
| 2012 | P-3B | MCoRDS v2 | High | 88 278 | 34 791 | 23 192 | 26 | 22 270 | 64 | -472 |
| 2013 | P-3B | MCoRDS v3 | Medium | 41 494 | 11 663 | 16 484 | 40 | 7 011 | 60 | -9 473 |
| 2014 | P-3B | MCoRDS v3 | High | (88 893) | 35 460 | N/A | | 26 374 | 74 | +26 374 |
| 2015 | C-130H | MCoRDS v5 | Medium | (71 291) | 450 | N/A | | 346 | 77 | +346 |
| 2016 | WP-3D | MCoRDS v5 | Medium | (27 134) | 250 | N/A | | 248 | 99 | +248 |
| 2017 | P-3B | MCoRDS v3 | High | (78 841) | 19 805 | N/A | | 13 229 | 67 | +13 229 |
| 2018 | P-3B | MCoRDS v3 | Medium | (42 189) | 2 000 | N/A | | 1 397 | 70 | +1 397 |
| 2019 | P-3B | MCoRDS v3 | Medium | (59 419) | 18 732 | N/A | | 17 016 | 91 | +17 016 |
| Total | | | | 482 902 (850 669) | 248 758 | 160 233 | N/A | 170 823 | N/A | +10 590 |

80 ^a See MacGregor et al. (2021) for additional detail on deployed aircraft.

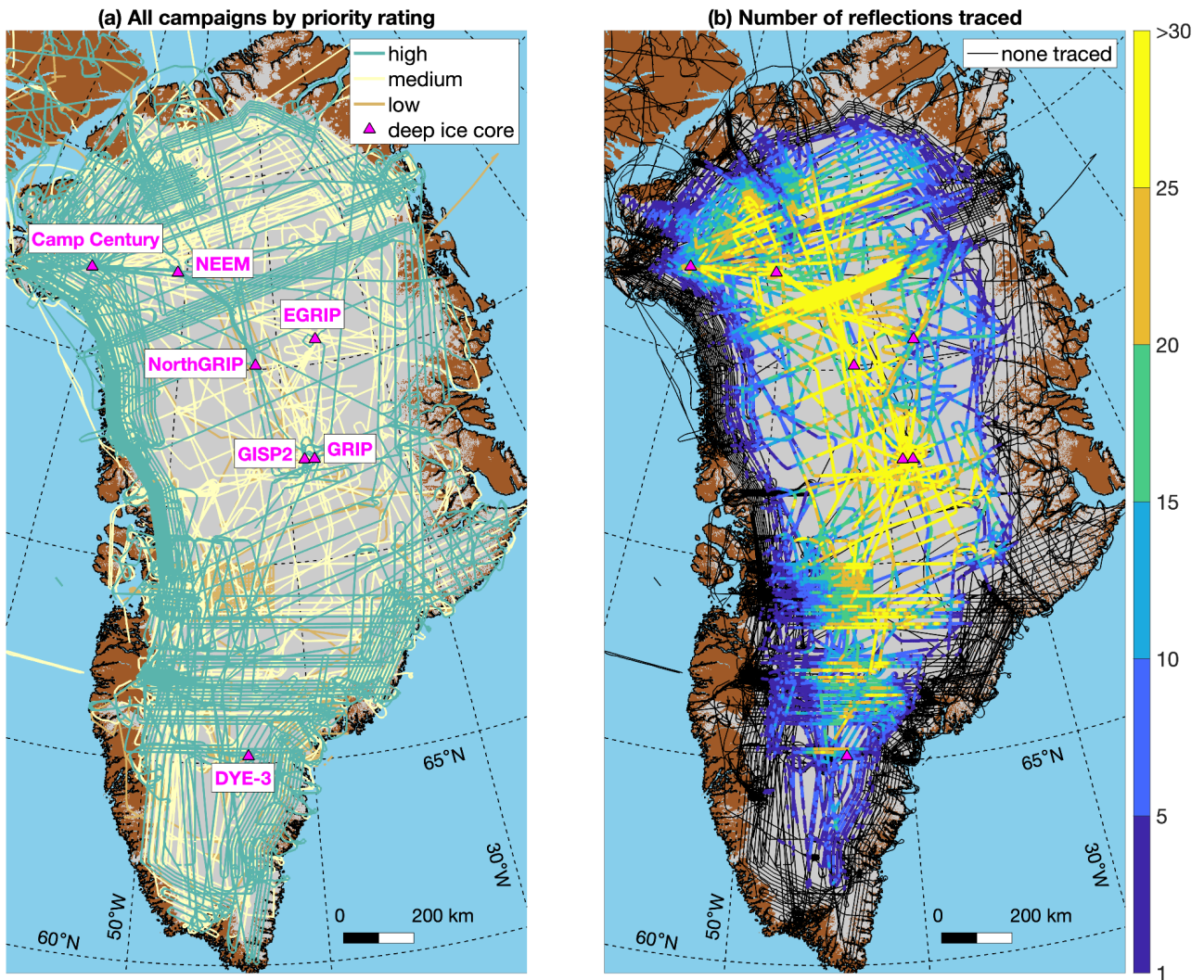
81 ^b Radar sounder nomenclature follows KU/CRISIS nomenclature. They maintain a document that details system characteristics for all its
82 surveys before 2010 (https://data.cresis.ku.edu/data/rds/rds_readme.pdf).

83 ^c The qualitative priority rating is described in §2.

84 ^d Total length evaluated includes all segments where the radar sounder was acquiring data, which sometimes includes segments that primarily
85 overflow Arctic sea ice that is not relevant to this study. Gaps within segments are common in earlier campaigns (1993–2001) and complicate
86 length calculations, so here we ignore gaps greater than 10 times the median distance between traces for each segment, leading to generally
87 lower values for those earlier campaigns than reported by M15. Values in parentheses for v1 are campaigns that were not traced by M15
88 because they were either not yet available (2014) or had not been flown at the time (2015–2019). For this study (v2), the total length of the
89 reduced set for each campaign is reported.

90 ^e Number of 1 km segments with at least one reflection traced (same metric as M15). Percentages are of the portion of the dataset evaluated,
91 which differs between M15 and this study.

92



93

94 **Figure 1:** Airborne radar-sounding surveys collected across the GrIS by KU/CRISIS between 1993 and 2019. Segments are color-coded by
 95 (a) priority rating and (b) maximum number of reflections traced within 1 km segments along-track. Ice, land, and ocean masks are from
 96 Howat et al. (2014) via BedMachine v5 (Morlighem et al., 2022).

97 The two-way traveltimes of both the air–ice and ice–bed reflections have already been traced and recorded in these data
 98 by semi-automated algorithms and quality-controlled (*QC'd*) by KU/CRISIS personnel; the difference between these
 99 traveltimes has been used extensively by others to map ice thickness across Greenland (e.g., Morlighem et al., 2017, 2022).
 100 The ice–bed reflection is harder to trace confidently than the air–ice reflection, and during our examination of the dataset we
 101 occasionally observed possible errors in the former. However, because we are primarily interested in reflection depths, we
 102 only adjusted the air–ice reflection traveltime to address minor but obvious errors that we observed in a very small portion of

103 the dataset that we evaluated (<0.1%). As for M15, when converting two-way traveltime t to depth, we assume that the radio-
 104 frequency real part of the relative permittivity of ice is 3.15, equivalent to a one-way radio-wave speed in ice of $168.9 \text{ m } \mu\text{s}^{-1}$.

105 A fundamental difference between M15 and this study revolves around the handling of “repeat-track” flights. This
 106 difference arises from the recognition that the lead priority for most NASA airborne surveys of the GrIS by OIB and its
 107 predecessors was detecting elevation change of the surface of the GrIS using laser altimetry along the same flight tracks
 108 repeatedly (e.g., Krabill et al., 2000; Csatho et al., 2014). In other words, many NASA flights that collected high-quality VHF
 109 radar-sounder data across the GrIS did so along a track that was nearly identical to another flight that did the same. M15
 110 ignored this issue and evaluated all 1993–2013 data, which complicated subsequent reconciliation of traced reflections into an
 111 ice-sheet-wide radiostratigraphy. For example, minor variations in flight track can lead to numerous intersections of two
 112 slightly different flights, which increases the potential for incorrect matches, and having numerous closely spaced reflections
 113 can bias subsequent 2-D gridding at the ice-sheet scale. In this study, we explicitly avoid tracing repeat tracks by first collating
 114 what we term the *reduced set*. To collate this reduced set, we first assign each campaign a priority rating (Table 1), i.e., an *a*
 115 *priori* qualitative assessment of the campaign’s overall radar data quality intended to guide prioritization for further tracing.
 116 This rating was mostly based on the radar system used and known campaign outcomes, but we recognize that individual intra-
 117 campaign segment quality can vary significantly due to several factors (e.g., environmental RF noise, data-acquisition
 118 interruptions, survey altitude change, GNSS or system-timing errors). We then manually inspected a map of the GrIS showing
 119 all radar flight tracks and identified all contiguous sets of frames required to “complete” a GrIS radiostratigraphy from the
 120 1993–2019 KU/CReSIS data. If any portion of a track was repeated, then only a portion from the campaign with the highest
 121 available priority rating was included. While this approach means that many previously traced segments from v1 of the GrIS
 122 radiostratigraphy have been effectively discarded, it minimized the work required to review those data. As a result, M15 traced
 123 at least one reflection in ~33% of the total dataset it examined, while this study more than doubled that ratio (69%; Table 1).
 124 Table 2 summarizes this step and all other major methodological differences between M15 and this study.

125

126 **Table 2:** Summary of key differences between the development of v1 (M15) and v2 (this study) GrIS radiostratigraphy datasets.

| Element | v1 (M15) | v2 (this study) |
|-----------------------|---|---|
| Data selection | All frames from 1993–2013 were investigated. | Campaigns were initially prioritized (Table 1) and then the “reduced set” of non-overlapping frames from 1993–2019 was identified manually based on geolocation and visual assessment of segment quality. Only this reduced set was investigated. |
| Data pre-processing | Individual frames were reconstituted into ~50 km-long radargrams (“blocks”) with ~1 km overlap on both ends for automated matching of reflections between them. | Individual frames were concatenated, regardless of length, and any pre-existing overlap between them (non-unique traces) was removed. |
| Reflection prediction | If complex radargrams were available, then phase-tracking was used; if not, then image processing | Only ARESELP was used to predict reflections and only for previously untraced segments from 2014–2019. |

(ARESP) was used, with the option for manual reflection prediction if both those methods failed.

| | | |
|-------------------------|--|---|
| Radargram visualization | Original (two-way traveltime), free-air-removed (“depth”) or reflection-flattened radargram views available. | Additional thickness-normalized view available where both ice–surface and ice–bed reflections were already traced. |
| Reflection selection | As many contiguous reflections as observed were selected to be traced. | Distinct and isolated reflections from the upper 80% of the ice column were prioritized for tracing, as these were assumed to be isochronal. |
| Reflection tracing | Semi-automatic peak following or manual tracing was used, with no cutoff length for the traced reflection. | Semi-automatic peak following was used, with an adjustable cutoff length (typically 10–100 km) to limit erroneous excursions and an automatic stop upon intersection with an existing traced reflection. |
| Reflection flattening | Either predicted or traced reflections could be used to flatten the radargram for QC and further tracing. | The flattening algorithm was adjusted to consider traced length (indicative of overall quality) rather than just the maximum number of traced reflections to identify the reference location, and it was improved to iteratively predict the depth of reflections not observed at the reference location (where they overlapped with other reflections that did). |
| Reflection tracing QC | Once all blocks for a given segment were traced, they were merged and displayed in a separate graphical user interface (<i>GUI</i>) for QC. | No additional merging was necessary; after any reflection was traced or adjusted, the GUI required that the sign of the depth difference between each reflection pair be the same throughout the radargram, i.e., that all reflections be stratigraphically conformable with respect to each other. |
| Reflection matching | Reflections were matched manually using a combination 2-D/3-D GUI, which were then QC’d using network graphs to check for reflection overlap. | Reflections were initially matched automatically based on their depths and the range resolution of the segment’s radar system; these matches were then manually QC’d and supplemented using a 2-D-only GUI. |
| Firn correction | None applied but a 10 m uncertainty in reflection depth was assumed. | For each trace, the modeled firn air content closest to the acquisition date was used to estimate the firn correction, and the assumed reflection depth uncertainty was reduced to 5 m. |
| Reflection dating | All six available deep ice cores were used to date reflections that intersected those cores; reflections that were matched to those core-intersecting reflections were dated, and the ages of remaining undated reflections were vertically interpolated where possible. | No major changes, except for the addition of EastGRIP ice core. |
| Reflection gridding | Normalized isochrone depths were gridded using ordinary kriging onto a 1 km grid. | Similar gridding method but using absolute isochrone depths and onto a 5 km grid, then smoothed. |

127

128

129

130

131

132

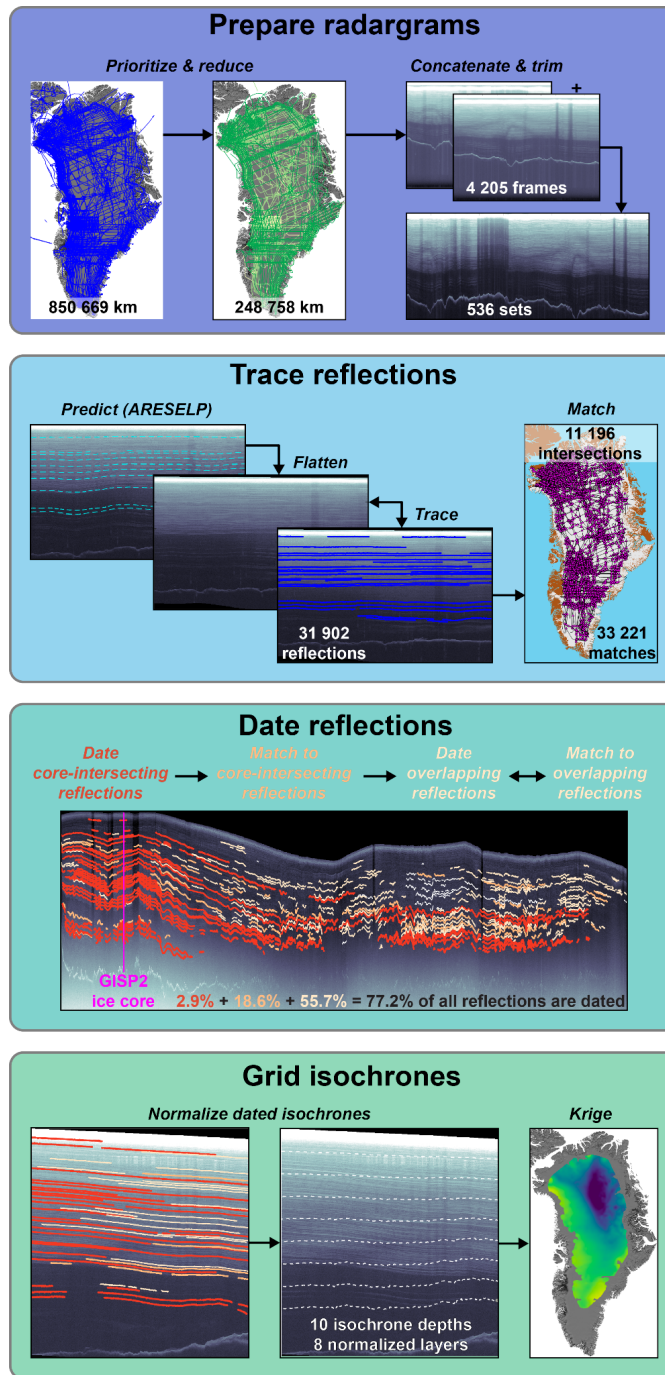
To ensure the continuity of traced reflections within individual segments and reduce the computing resources required, M15 reconfigured individual radar data frames so that they partly overlapped with each other (typically by ~1 km). However, this process often created more challenges than it solved. In the intervening decade since that study, available computing resources have grown substantially but the data volume of any given SAR-processed segment from the radar systems deployed has remained the same. Here we simply concatenate contiguous sets of frames (portions of segments) as needed for the reduced

133 set, removing any non-unique traces that are present (whether in time or space). This procedure resulted in 536 sets of
134 concatenated radar data frames that range between 12–3774 km long, with a median length of 250 km. We ultimately traced
135 at least one reflection in 496 (93%) of those concatenated sets (Fig. 2a).

136 **3 Reflection analysis methods**

137 In this section, we describe the methods we used to trace GrIS radiostratigraphy, QC and date the dataset, focusing primarily
138 on the key differences between this study and M15, all of which were made with the intent of accelerating product development
139 and decreasing uncertainty therein. Table 2 summarizes those key differences in our methodology for pre-processing,
140 predicting, tracing, QC'ing, dating and gridding GrIS radiostratigraphy. Fig. 2 shows the key elements of this workflow.

141



142

143 **Figure 2:** Flowchart illustrating the key steps involved in generating GrIS radiostratigraphy v2. Values given relate to the entire dataset, not
 144 just the radargrams shown. (a) Radargram preparation, including selection of the reduced set and concatenation (§2). (b) Typical tracing
 145 workflow and subsequent inter-segment reflection matching (§3.1, 3.2). (c) Reflection dating begins at ice cores, is sequentially propagated
 146 outward using reflections matched core-intersecting ones, and then any remaining reflections that horizontally overlap with already-dated
 147 ones are then dated where possible. The latter two steps are then repeated until no new reflections are dated. White reflections are undated

148 (§3.3) (d). Gridding isochrones begins by vertically interpolating the dated radiostratigraphy to pre-selected ages/depths, and then each of
149 those ages/depths are gridded two-dimensionally using ordinary kriging (§3.3).

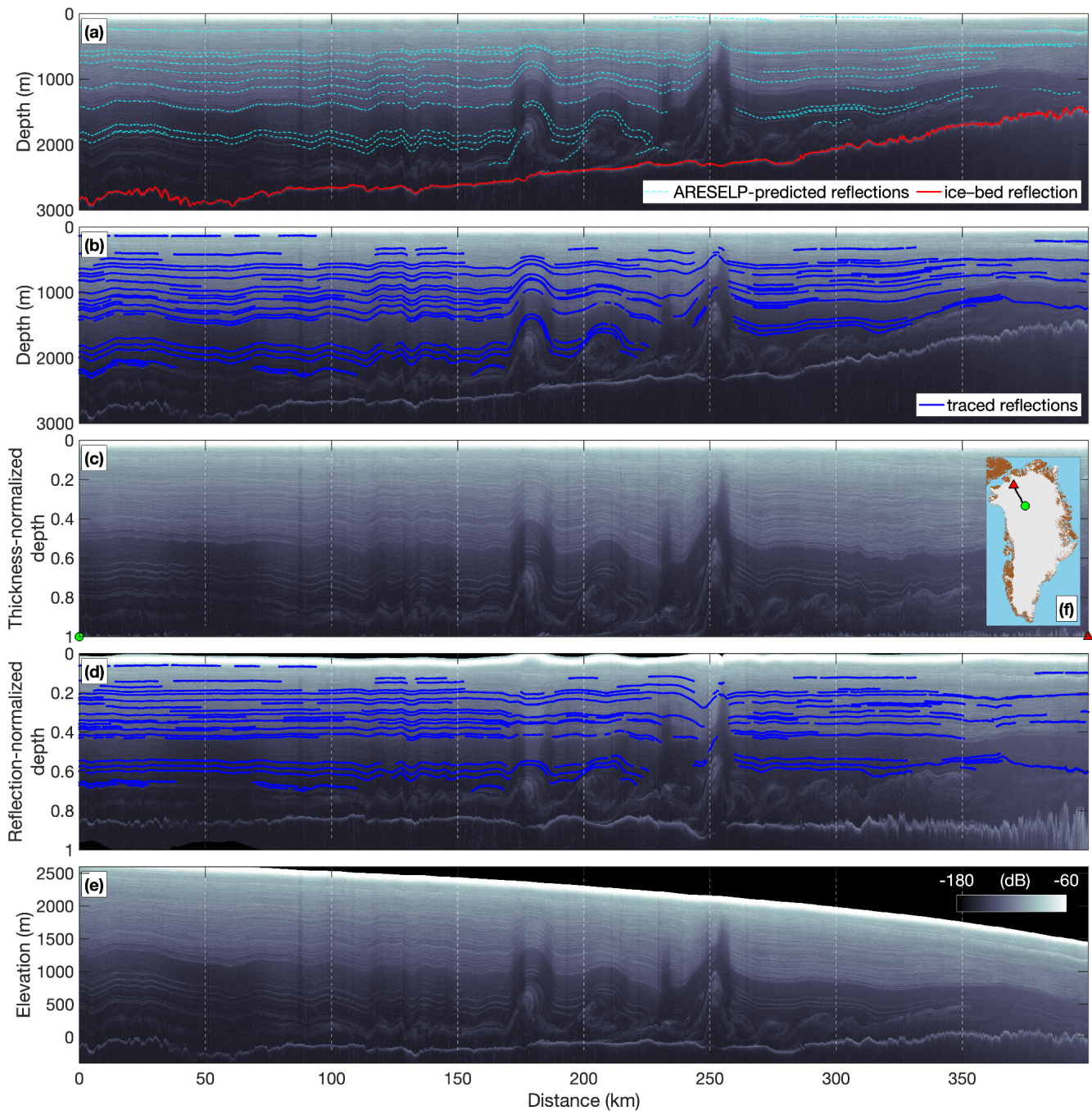
150

151 **3.1 Tracing workflow**

152 It is much simpler to confidently trace any reflection if a prediction of its location can be generated automatically beforehand.
153 M15 introduced two automatic methods that leveraged the phase change of the recorded complex signal to predict the slope
154 of internal reflections and – by integrating these slopes along-track – the shape of the reflections themselves. However, these
155 methods were limited by the availability of large-volume, single-channel complex data from KU/CReSIS, and they cannot be
156 applied to data that has already been SAR-focused. In cases where complex data were not available (i.e., most of the 1993–
157 2013 dataset), Automated Radio Echo Sounding Processing (*ARESP*) was applied, using a refactored version of the *ARESP*
158 algorithm introduced by Sime et al. (2011). However, all three methods focus on estimating reflection slope, as do similar
159 methods introduced later (e.g., Holschuh et al., 2017). As a result, it is often difficult to determine where to automatically
160 terminate a given reflection prediction in a manner comparable to that which often occurs with observed reflections, e.g., they
161 fade out or merge with another reflection. This challenge tends to limit the use of slope-prediction methods to well-behaved
162 radargrams with stable and relatively high signal-to-noise ratios.

163 Alternatively, Xiong et al. (2018) introduced an alternative method that they termed the Automated RES Englacial Layer-
164 tracing Package (*ARESELP*). This method first identifies candidate reflection peaks vertically using wavelet transforms, prior
165 to then propagating these candidate reflection peaks horizontally using Hough transforms for slope prediction. We selected
166 this method for reflection prediction in previously untraced campaigns (2014–2019): 1. It does not require complex data; 2. It
167 permits reflections to terminate; 3. It often generates realistic synthetic radiostratigraphy; and 4. The algorithm was publicly
168 archived. We refactored the *ARESELP* algorithm (written in MATLAB™) to both accelerate it and improve QC of its output;
169 we then applied it to the 2014–2019 campaigns (Figs. 2b, 3a). Despite our improvements, *ARESELP* is only used to predict
170 reflection geometry and not as a substitute for tracing itself, as its output quality is variable (Jebeli et al., 2023). For example,
171 *ARESELP* often identifies the multiple of the air–ice reflection as a candidate internal reflection. Where *ARESELP* is
172 successful, its outputs were used only to initially “flatten” the radar data (described below) and then discarded, so that no
173 *ARESELP*-predicted reflections were mistaken for operator-traced ones.

174



175

176 **Figure 3:** Multiple visualizations of a portion of a single segment (8 concatenated frames) from 2017-04-13 (20170413_01_049–056) that
 177 approximately follows ice flow from a central ice divide toward the outlet of Petermann Glacier. All radargrams shown at the same color
 178 scale. (a) Untraced radargram in terms of depth, i.e., the variable-length portion of the radargram before the air–ice reflection has been
 179 removed, with ARESELP-predicted reflections overlain. (b) Same as (a) but with traced reflections overlain. (c) Thickness-normalized
 180 radargram. (d) Reflection-flattened radargram. (e) Elevation-corrected radargram (relative to geoid). (f) Location of radargram in Greenland.

181 As illustrated by M15, flattening radar data with respect to predicted or already-traced reflections is both a valuable QC
 182 method and one which can accelerate further tracing (Figs. 2b, 3d). Here we continue to use this method with minor adjustments
 183 that permit it to more reliably and iteratively estimate the vertical position of reflections that were not observed at the reference
 184 location, but which overlap with ones that were. However advantageous, this flattening method requires that either predicted
 185 or traced reflections are already available, which is not always the case. Inspired by earlier studies concerned with the physical
 186 interpretation of radiostratigraphy and modeling thereof, especially Nereson et al. (1998) and Hindmarsh et al. (2006), here
 187 we introduce an additional radargram reprojection that is *thickness-normalized*, which requires only that the air–ice and ice–
 188 bed reflections already be traced, as is the case for nearly all the KU/CRISIS dataset we evaluated. Normalization by ice
 189 thickness is commonly applied in analytic and numerical models of ice flow to ease interpretation, but to the best of our
 190 knowledge it has not been applied previously to the returned power P_r displayed in radargrams themselves, even though it can
 191 accelerate tracing. In the nomenclature of Hindmarsh et al. (2006), thickness normalization of radargrams also offers a rapid
 192 way of evaluating whether internal reflections drape over subglacial topography (i.e., they are essentially a shallower and
 193 smoother version of the ice–bed reflection) or override it (i.e., variations in reflection depth bear little resemblance to the ice–
 194 bed reflection and are mostly negligible). Following thickness normalization, draping reflections should be flatter, while
 195 overriding ones could be rougher. In practice, because relatively few of the flight tracks considered here both follow present
 196 ice flow *and* contain interpretable radiostratigraphy (Sime et al., 2014; Cooper et al., 2019), such a straightforward
 197 glaciological evaluation (draping vs. overriding) is often difficult. We note that alternative physically based vertical
 198 reprojections of radar data are conceivable, such as the coordinate transform for ice-flow models described by Parrenin et al.
 199 (2006), but here we focus on the simplest to implement and interpret for reflection tracing.

200 To perform this thickness normalization, the surface and bed traveltimes, $t_s(x)$ and $t_b(x)$, respectively, are first smoothed
 201 using a 3-km-long locally weighted filter in the along-track direction x . The normalized depth coordinate \hat{z} is
 202 $(t - t_s(x))/(t_b(x) - t_s(x))$. Because $t_s(x)$ and $t_b(x)$ both vary along-track, the number of fast-time samples that form the
 203 radargram between them also varies, so the vertical interval between samples $\Delta\hat{z} = \hat{z}_{i+1} - \hat{z}_i$ also varies along-track. The
 204 thickness normalization is a vertical rescaling that does not directly alter the returned power $P(x, t)$ that constitutes the
 205 radargram, so if the vertical resolution of the displayed radargram can also vary along-track, then the thickness-normalized
 206 returned power $\hat{P}(x, \hat{z})$ can be displayed with no change in amplitude from $P(x, t)$. In practice, it is simpler and more
 207 computationally efficient to display two-dimensional ($2-D$) matrices with two monotonic axes. Thus, the second and final step
 208 is to vertically interpolate $P(x, t)$ onto a single monotonic \hat{z} vector that has the same number of samples as the original
 209 radargram and ranges from 0 to 1, which sometimes slightly degrades the signal-to-noise ratio of $\hat{P}(x, \hat{z})$ relative to $P(x, t)$.
 210 As for reflection-based flattening, reflection traveltimes can be similarly vertically reprojected, or traced within this projection
 211 and then reprojected to the radargram’s original vertical frame of reference (t). This reprojection is simpler than that for
 212 reflection-based flattening, is also parallelizable, and it is particularly valuable for initial reflection tracing within radargrams
 213 where $H(x)$ varies substantially, as it reduces the need to adjust the vertical axis when tracing.

214 In terms of selecting which reflections to trace, for v2 we focused exclusively on those that we deemed most likely to be
215 isochronal. Specifically, we focused on distinct, relatively isolated reflections in the upper ~80% of the ice column that are
216 observed across many radargrams, are not diffuse (i.e., difficult to trace using semi-automatic peak following), and do not
217 form part of a disrupted basal unit. While the above criteria represent an effort to ensure the validity of a core assumption of
218 our approach (reflection isochroneity), we are not aware of direct observations of unconformable reflections that are both
219 within the GrIS interior and above disrupted basal units that contradict this assumption, as have been observed in Antarctica
220 (e.g., Das et al., 2013). Deeper basal ice in the GrIS interior and strata exposed at the ice margin can clearly be disrupted,
221 overturned and probably unconformable (Dahl-Jensen et al., 2013; MacGregor et al., 2015a, 2020; Panton and Karlsson, 2015;
222 Bons et al., 2016; Leysinger-Vieli et al., 2018), so we mostly avoid tracing reflections within this zone unless they meet other
223 criteria and are identifiable across a large distance or several radargrams. As a result, several deeper reflections mapped by
224 M15, which were typically the top of disrupted basal units, were removed during our review of the v1 dataset.

225 We continue to use semi-automatic peak following to trace reflections, typically using a very narrow fast-time (vertical)
226 sampling window (± 1 sample; 1.7–5.3 ns, equivalent to 1.4–4.5 m, depending on campaign) between traces, but sometimes
227 ± 2 samples and rarely ± 3 samples for especially steep reflections. The algorithmic speed of this method outweighs its relative
228 simplicity, as it permits faster tracing *and* faster correction of inevitable errors therein. To limit these errors, we terminate
229 propagation of a candidate reflection automatically once another existing reflection is intersected or where tracing has
230 propagated a prescribed distance limit from the manually selected inception (typically 25–100 km, depending on radargram
231 quality and reflection slope) – whichever is first.

232 A critical addition to the tracing workflow relative to M15 is an algorithmic check for stratigraphic conformability
233 following the tracing of any reflection or modification thereof. This QC check simply requires that the sign (either >0 or <0)
234 of the depth difference between any pair of reflections be both non-zero and the same throughout the radargram. In other
235 words, no traced reflection can be both above and below another. This check automatically identified occasional tracing errors
236 in the v1 radiostratigraphy that we rectified, and it simplified the process of QC'ing v2. Once tracing is complete, all reflections
237 were vertically re-adjusted by $\leq \pm 1$ fast-time (vertical) sample to match the local maximum in P_r . This adjustment also increases
238 the value of recorded reflection P_r values for future investigations (e.g., MacGregor et al., 2015b).

239 **3.2 Inter-segment matching**

240 Once tracing was complete, intersections between traced segments were identified automatically, with an algorithm that
241 requires a minimum intersection angle of 5° between segments in map view and limits identified intersections to a maximum
242 along-track density of 5 km within any given segment. The combination of the reduced set and these intersection selection
243 criteria generated 24% fewer intersections than v1 (11 196 vs. 15 148), which simplifies subsequent reflection matching (Fig
244 2b). Assuming a uniform reflection matching error rate, fewer matching errors will be made if there are fewer intersections to
245 evaluate.

246 Matching reflections between traced segments and between distinct radar systems is a significant challenge for large
247 radiostratigraphic datasets. While M15 evaluated automatic matching, they ultimately did not use it. Here we generate an initial
248 set of reflection matches automatically, with an algorithm that limits inter-segment matches to those with a mean depth
249 difference no more than three times the maximum range resolution of the segment pair’s radar system (2.4–4.4 m for most
250 systems considered) within 500 m of their intersection. These automatic matches were then QC’d using network graphs to
251 verify stratigraphic conformability between reflection pairs, using an algorithm like that applied when tracing individual
252 segments (§3.1), i.e., if a segment contains two reflection that overlap horizontally, then they cannot both be matched to the
253 same reflection in another segment. Additional matches were then identified manually, which were then again QC’d using
254 network graphs. In M15, matches were not permitted between the earliest campaigns (1993–1997) and later ones due to their
255 difference in range resolution; here we permit such matches as prominent traced reflections were often similar across all
256 campaigns.

257 **3.3 Dating and gridding**

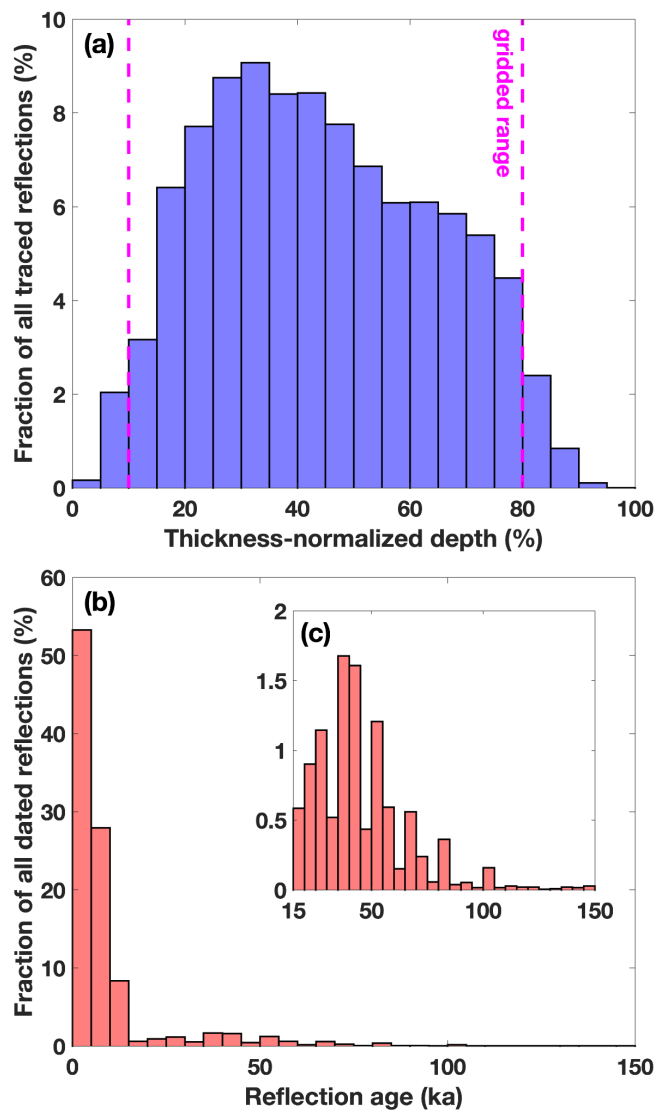
258 Once traced, matched and merged, reflections must be dated to be of maximum value to the broader scientific community.
259 Our dating algorithm is mostly unchanged from M15, to which we refer the reader for further details. We are unaware of any
260 substantive improvement in reflection dating methodology developed since then, although alternatives exist if better estimates
261 of accumulation histories or modern dielectric profiling ice-core data are available (Cavitte et al., 2021; Franke et al., 2025).
262 To date traced radar reflections across an ice sheet, multiple dated and synchronized ice cores are required. We use the same
263 six deep ice-core depth–age scales as M15 (their Table 2) but supplement them here with the addition of the partially complete
264 EastGRIP (*EGRIP*) depth–age scale from Mojtabavi et al. (2020). This depth–age scale includes the upper 1884 m of the ice
265 column – approximately three quarters thereof given an ice thickness of ~2550 m – which records the period 0–15 ka.
266 Compared to M15, we slightly relax the search radius within which a radar segment is considered to have “intersected” an ice
267 core from 3 to 5 km, increasing the number of core intersections from 53 to 65. The use of the reduced set (no repeat tracks)
268 also decreases dependence on the Camp Century ice core, which was overrepresented in the v1 dataset (47% of all intersections,
269 as compared to 31% in this study). We continue to use the “quasi-Nye” dating method introduced by M15 to vertically
270 interpolate the age of undated reflections that are either sandwiched between or are vertically near pairs of dated reflections
271 (no more than the thickness of a dated layer pair or 20% of the ice thickness, whichever is less). This method seeks the best-
272 fit vertical strain rate that can match the depth–age relationship of the two bounding reflections and then uses this vertical
273 strain to interpolate the age of the undated reflection – or extrapolate where appropriate (Fig. 2c).

274 Previously, an undated reflection could only be dated if it did not cause the vertical profile of age anywhere in the segment
275 to decrease with depth. Here we relax this requirement slightly to accommodate potential matches of vertically closely spaced
276 reflections by instead requiring that the age of the putative dated reflection be within 5% of the uncertainty in age of adjacent
277 dated reflections. This relaxation accommodates slight mismatches in age between reflections that intersect different ice cores.
278 Finally, where sufficient dated reflections exist, we use quasi-Nye interpolation to estimate the along-track depth of a set of

279 “synthetic” isochrones at predetermined ages. We include the same set of five ages generated by M15 (9, 11.7, 29, 57 and 115
280 ka) along with five more of additional paleoclimatic interest from the Late and Early Holocene, the bounds of the Bølling-
281 Allerød period during the Last Glacial Period, and an approximate Last Glacial Maximum (3, 8, 12.8, 14.7, and 19 ka;
282 Rasmussen and others, 2006).

283 Like M15, we use ordinary kriging to grid the depths of the 1-D along-track isochrones onto a 2-D grid using the Python
284 geostatistical simulation software package GStatSim (v1.0.6; MacKie et al., 2023). We also use quasi-Nye interpolation (M15)
285 to infer the age at predetermined thickness-normalized depth intervals along all traced segments and then grid these ages as
286 well. We select a 5 km grid in the standard EPSG:3413 projection – rather than 1 km as in M15 – to focus on the large-scale
287 age structure of the ice sheet. Contrary to M15, we find that absolute depths are smoother at large scale than thickness-
288 normalized depths, so we grid the former instead. We find that a zero-nugget spherical semivariogram model is a better
289 representation of the experimental semivariogram of shallower/younger isochrones (≤ 19 ka), while an exponential model is
290 better suited to deeper/older ones. For the age at regular depth intervals, we restrict the gridding to the middle 70% of the ice
291 column (10–80% ice thickness) at 10% intervals as this depth range captures the range of most traced reflections (Figs. 2d, 4);
292 we find that spherical variograms are most suitable at all depths. This normalized depth range is more conservative than for
293 M15 (4–100% ice thickness at 4% intervals). Independent variogram models are applied to each depth/age, as opposed to a
294 single variogram model as in M15. We apply a 2-D Gaussian smoothing filter to all the resulting grids to reduce noise from
295 individual traced segments and fill in small, enclosed gaps using natural neighbor interpolation. Finally, we blank out any
296 portions of the grid that would result in age overturning (unconformities) relative to other adjacent grids.

297



298

299 **Figure 4:** (a) Histogram of the normalized depth of all traced reflections (both dated and undated). Vertical magenta dashed lines highlight
 300 the normalized depth range for which the age of the ice sheet is gridded. (b) Histogram of the age of dated reflections. (c) Zoom-in of panel
 301 b on the pre-Holocene age range.

302 3.4 Depth and age uncertainty estimation

303 The depth uncertainty of the traced reflections is principally attributable to the assumed radio-wave velocity in pure ice
 304 and a correction for spatiotemporally variability firm air content. As for M15, we assume that the real part of the radio-frequency
 305 complex relative permittivity of pure ice ϵ'_{ice} is 3.15, equivalent to a radio-wave velocity in ice v_{ice} of $168.9 \text{ m } \mu\text{s}^{-1}$. M15 did
 306 not directly apply a firm correction and instead attributed a constant and uniform 10 m depth uncertainty to all traced reflections.
 307 Since then, substantial progress has been made in the modeling and validation of the firm air content in the near-surface of ice

308 sheets, due to its importance for interpretation of satellite altimetry data (e.g., Medley et al., 2022). The total firm air content is
309 equivalent to the firm correction that is commonly applied to radar-sounding data to correct reflection depths. Here we use the
310 modeled firm air content developed by Medley et al. (2022) for the period 1980–2021 across Greenland and Antarctica to
311 determine the local firm correction for each radar trace from the nearest 5-d simulation interval to the acquisition date. We then
312 assume that the reflection depth uncertainty associated with the firm correction is reduced to 5 m. The median modeled firm
313 correction applied is ~19 m, but it can be up to ~25 m.

314 The age uncertainty for each dated reflection is calculated following the same methods described in further detail by M15.
315 For core-dated reflections, this total age uncertainty is the combination of the reported uncertainties in the ice-core depth–age
316 scales (unchanged from M15), the depth uncertainty of the reflection (discussed above), and the uncertainty induced by the
317 range resolution of the radar system used. The latter quantity depends on the signal-to-noise ratio (*SNR*) of the reflection at its
318 closest approach to the ice core, which is typically ~5 dB, so for simplicity we assume that quantity is uniform for all core-
319 dated reflections. For reflections dated using quasi-Nye dating, an additional uncertainty is included that accounts for the
320 interpolation/extrapolation of age, which is based on the age uncertainties of the existing dated reflection pair and the variance
321 of the interpolated/extrapolated age across the overlapping section (Equation 12 in M15).

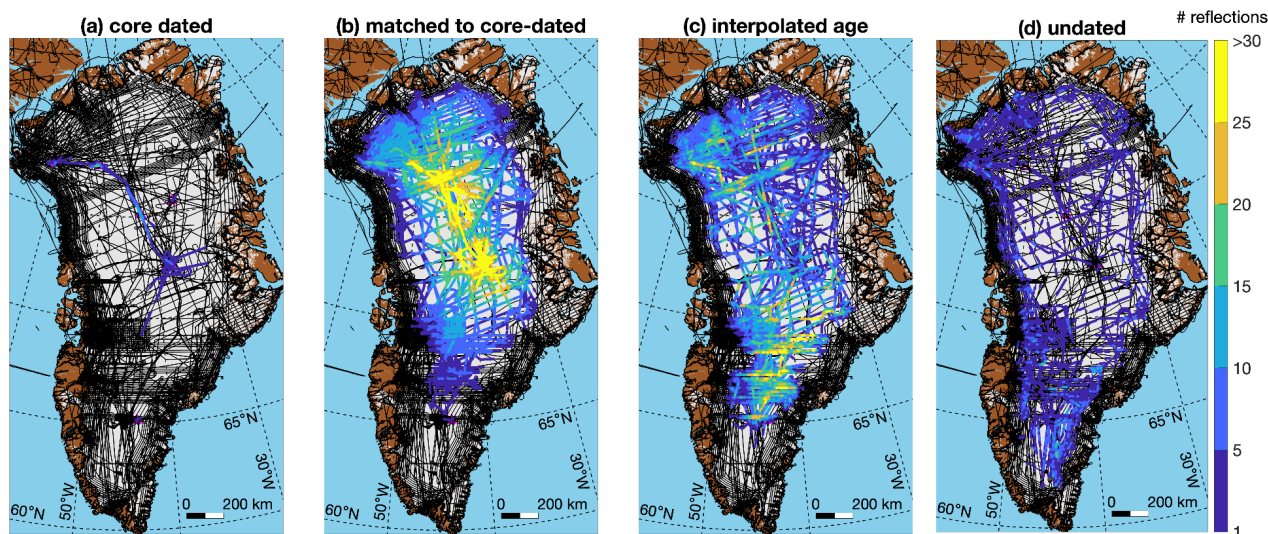
322 To estimate the uncertainty of the 2-D grids, we first also vertically interpolate the along-track depth (age) uncertainty of
323 dated reflections to the age (depth) of interest and then kriging these quantities using the same variogram model parameters as
324 for their respective age (depth) of interest. These kriging-derived uncertainties are then combined with the kriged uncertainty
325 for the parameter of interest (depth or age) as the square root of the sum of squares (M15 only considered the latter term).

326 **4 Results**

327 The generation of the reduced set, where we downselect repeat flight tracks to a single instance acquired with the highest-
328 fidelity radar system, substantially reduces the number of radargrams that must be examined to generate a complete GrIS
329 radiostratigraphy from NASA/NSF airborne radar-sounding data. For this second version of the radiostratigraphy dataset (v2),
330 we reviewed only 36% of the 1993–2013 radargrams, as compared to 100% for v1. However, we recorded a traced reflection
331 in 65% of the 1993–2013 radargrams examined (112 213 of 172 062 km), as compared to 33% for v1 (160 233 of 482 903
332 km). While we preserved fewer line kilometers of reflections for 1993–2013, we added 58 610 km from 2014–2019 acquired
333 using generally higher-fidelity radar systems.

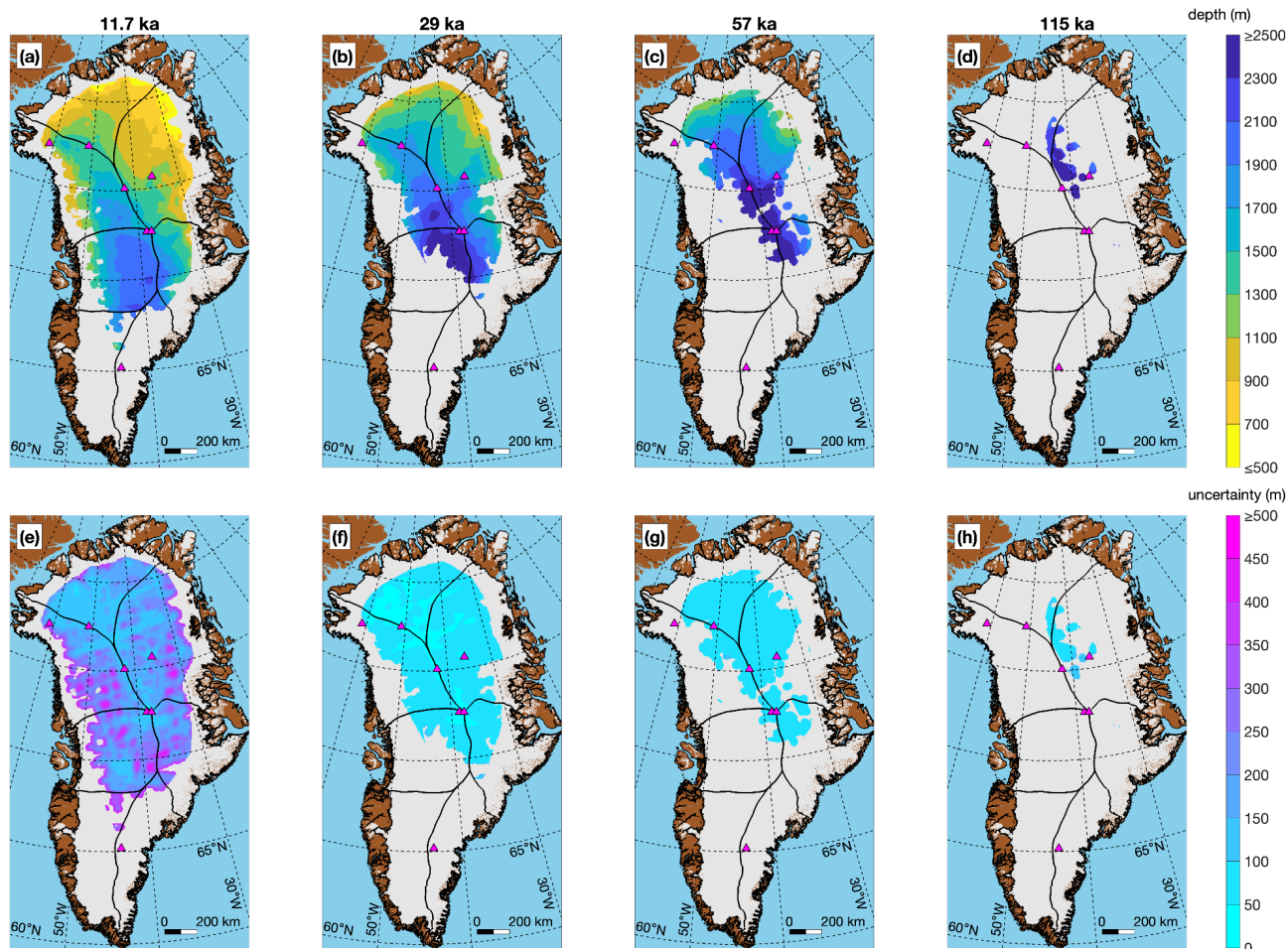
334 GrIS radiostratigraphy v2 contains 31 902 individual traced reflections of widely varying lengths. Of these reflections,
335 2.9% were dated “directly” where they intersected ice cores, 18.6% by automatically or manually identified matches to those
336 core-dated reflections, and another 55.7% using quasi-Nye dating, leaving 22.8% of traced reflections undated (Fig. 2c). Direct
337 core-dating of reflections is essential but – following our tracing strategy – results in a very limited spatial distribution of dated
338 reflections, mostly following the northern part of the central ice divide (Fig. 5). Reflections matched to those core-dated
339 reflections significantly expand the coverage of dated reflections, especially in central and northern Greenland. Farther south,

340 where reflections become discontinuous, age interpolation of dated reflections is especially important between $\sim 65\text{--}71^\circ\text{N}$.
341 Undated reflections remain mostly around the periphery of the GrIS, in fast-flowing regions such as Sermeq Kujalleq, and in
342 southern Greenland south of $\sim 68^\circ\text{N}$.
343



344
345 **Figure 5:** Number of traced reflections by the method in which they were dated.

346
347 For completeness and validation, we generated Movie S1, which shows all traced segments in an elevation-corrected
348 reference frame. This movie illustrates both the breadth of the traced reflections and the considerable number of *untraced*
349 reflections, which are typically discontinuous and less distinct – but not exclusively so. Most (94%) reflections were traced in
350 a depth range within 10–80% of the ice thickness, following both our stated prioritization, signal loss with increasing depth,
351 and the challenge of tracing distinct very shallow reflections within most of the KU/CReSIS dataset that we evaluated. The
352 large majority (86%) of all dated reflections are from the Holocene (11.7–0 ka; Fig. 3b), which is consistent with previously
353 observed patterns of radar reflectivity across the ice sheet. Some of the most distinct reflections are from the Last Glacial
354 Period (115–11.7 ka), in particular the well-known trio observed throughout northern Greenland (37.7, 44.7 and 50.7 ka,
355 respectively), so they are also often some of the most contiguous or readily matched between segments so they tend to be
356 under-represented in the distribution of all dated reflections compared to numerous and sometimes difficult-to-match shallower
357 Holocene reflections.

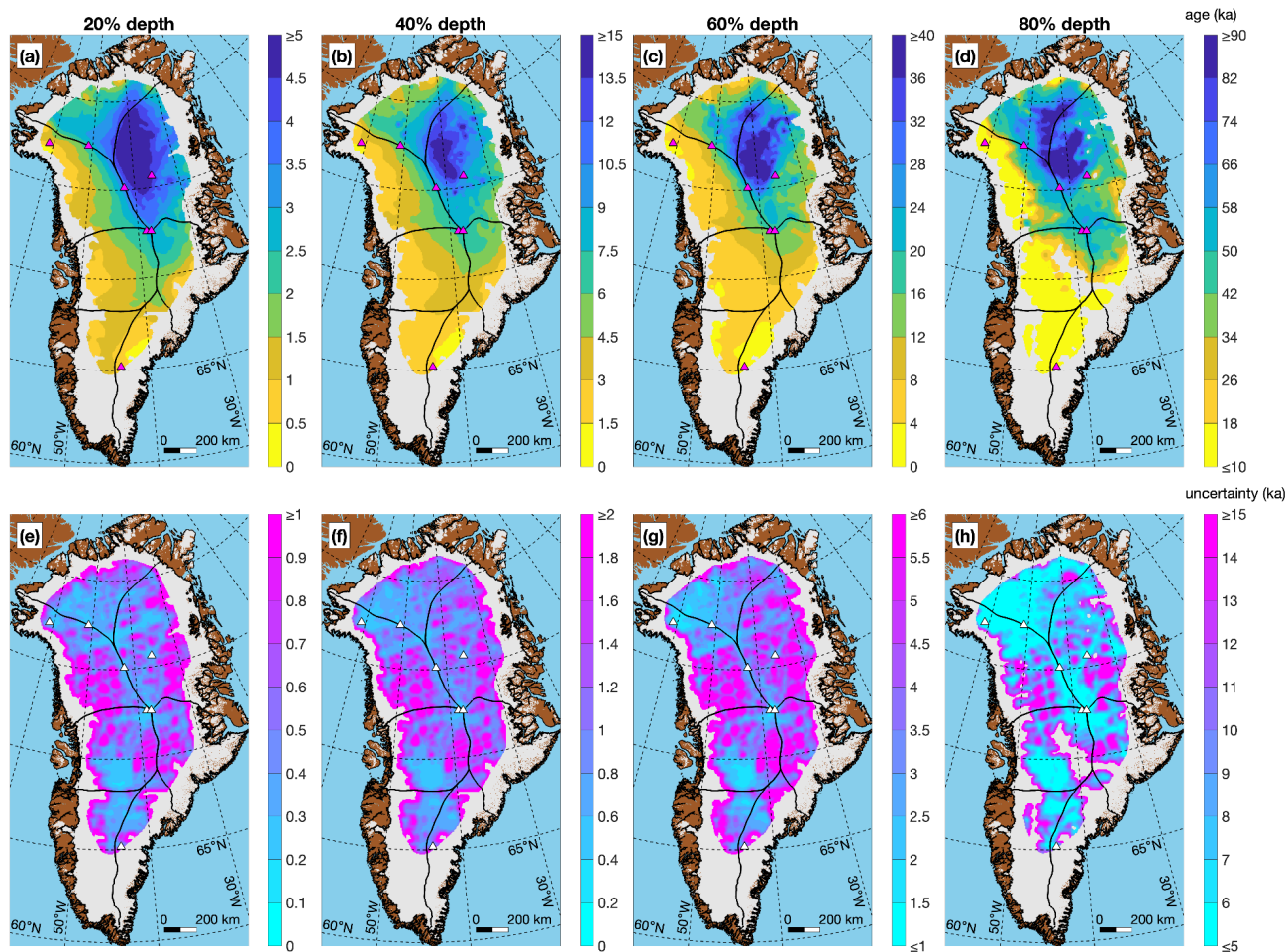


358
359
360

Figure 6: (a–d) Gridded depth of four out of the ten gridded synthetic isochrones (11.7, 29, 57 and 115 ka, respectively). (e–h) Gridded uncertainty in these isochrones. Ice drainage basins (black lines) are from Mougint et al. (2019).

361
362
363
364
365
366
367
368
369
370

The resulting depth/age grids cover up to 65% of the ice sheet by area (Figs. 6 and 7). The uncertainties in the resulting datasets also are slightly more completely expressed than by M15. In comparison to similar depth/age grids produced by M15, it is clear that producing a dated GrIS radiostratigraphy within ~ 100 km of the ice margin or south of $\sim 68^\circ\text{N}$ remains challenging. Neither version of the dataset does so consistently, except for v1 along parts of the northern margin of the GrIS, which we attribute to less conservative kriging parameters than those applied in this study. We attribute this broader challenge not to the sparsity of surveys (Fig. 1) but rather to the absence of traceable radiostratigraphy (less common) or the low continuity of observed radiostratigraphy (more common), which makes it less feasible to trace efficiently using this study's methods and was not prioritized (Movie S1). This result is consistent with earlier automated assessments of radiostratigraphic continuity by Sime et al. (2014) and M15, particularly in terms of where traceable radiostratigraphy is present (although not necessarily dateable).



371
372
373

Figure 7: (a–d) Gridded age of four out of the seven gridded ages at 20, 40, 60 and 80% of ice thickness, respectively. (e–h) Gridded uncertainty in these ages. Note each panel has a different color scale, whereas for each row of Fig. 6 the color scale is the same.

374
375
376
377
378
379

As observed by M15 and reproduced here, the oldest ice at most depths is observed in the southeastern portion of the northernmost ice drainage basin and the northwestern portion of the northeastern drainage basin (northwest of the Northeast Greenland Ice Stream). Any potentially conformable Eemian ice (130–115 ka) is likely also located there (Fig. 6d). These results are qualitatively consistent with observations of outcropping pre-Holocene along the northern margin of the GrIS (MacGregor et al., 2020). Any substantial (>100 m) conformable layer of pre-Holocene basal ice is likely absent south of ~65°N, which is consistent with the higher long-term accumulation rates there (e.g., MacGregor et al., 2016a).

380
381
382
383
384

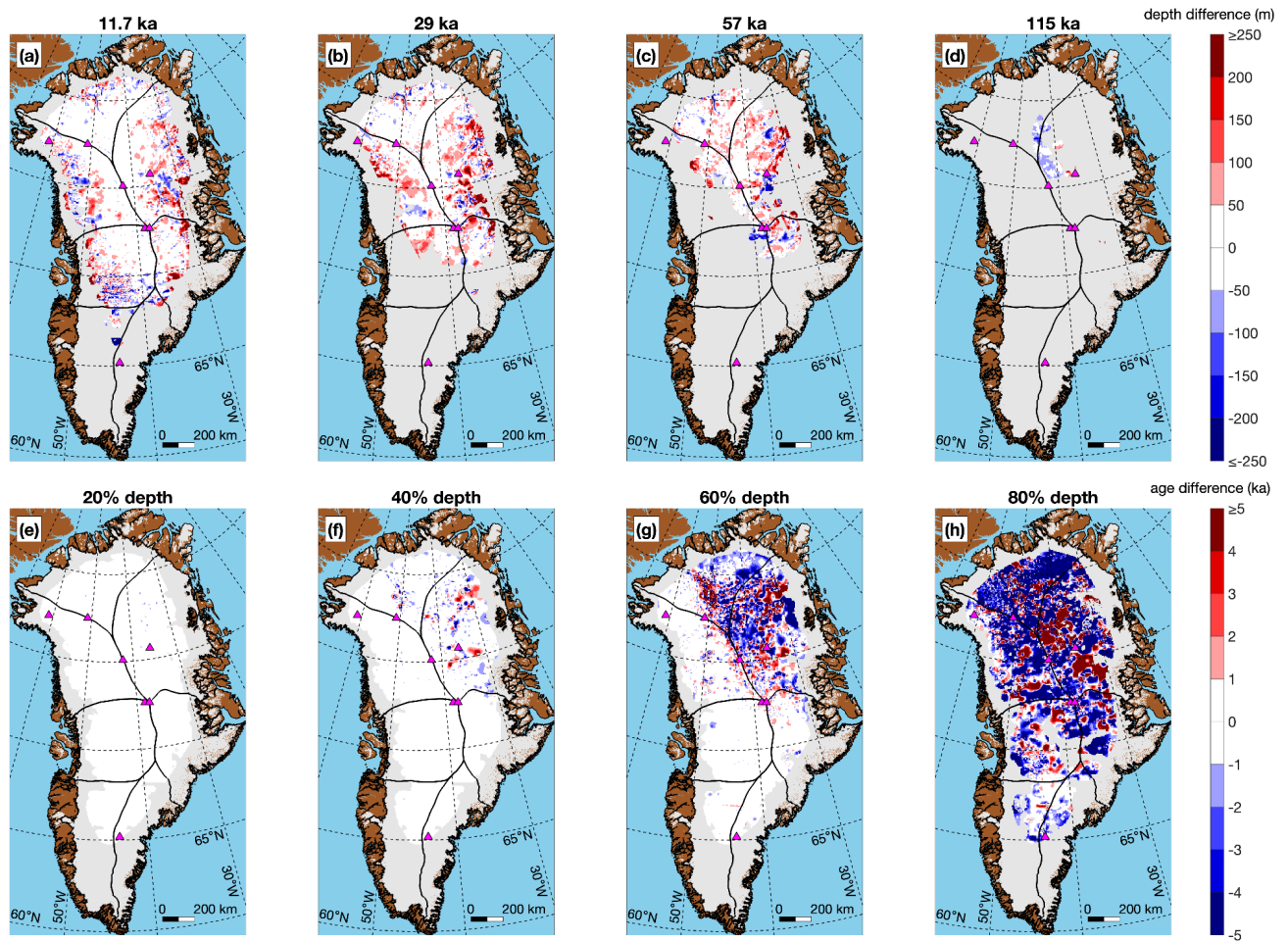
The gridded uncertainty of the synthetic isochrones (Fig. 6e–h) varies significantly and does not necessarily increase with depth. Assuming comparable relative uncertainties for all dated reflections, it also depends on proximity (in age) of the synthetic isochrone to dated reflections. While reflections were regularly traced near the onsets and terminations of the Bølling-Allerød period (14.7–12.8 ka), the Younger Dryas cold period (12.8–11.7 ka) and the Holocene epoch (11.7 ka–present), much more common are yet younger reflections (Fig. 4a) from which the depth of those onsets/terminations were sometimes

385 estimated. In contrast, the prominent trio of older reflections mentioned above that are often observed together in the northern
386 GrIS represent a more spatially limited but stronger constraint on the location of some older climate transitions (e.g., Fig. 4f,g).

387 This study's gridded fields are generally similar to those in M15 (Fig. 8). We attribute most differences to improved
388 coverage and QC in this study, the more conservative coarser grid resolution (5 km vs. 1 km) and the final smoothing applied.
389 For the isochrone depths, as expected the differences increase toward the ice margin and away from ice core sites with a slight
390 trend toward increasing magnitude with increasing isochrone age. The gridded age differences display a more complex spatial
391 pattern. Their differences are lower at shallower depths, as expected, but increase significantly at 60% depth particularly in the
392 older northern and northeastern drainage basins. At 80% depth – the maximum normalized depth we considered – the
393 magnitude of the differences is large but varies in sign, with an increasing magnitude trend toward the north.

394 Franke et al. (2023) presented multiple gridded isochronal datasets for the northern GrIS from OIB and other campaigns
395 led by the Alfred Wegener Institute (*AWI*), which could be compared to our gridded products. However, because they gridded
396 directly traced isochrones, rather than the synthetic isochrones at climate transitions that we focused on, based on the ages of
397 their isochrones alone most of our gridded isochrones are not directly comparable with theirs. Only one is potentially
398 comparable with our 11.7 ka isochrone (Fig. 8a), which is their 12.0 ka isochrone for the Petermann Glacier onset region.
399 However, given the two-order-of-magnitude difference in grid resolution between their isochrone (0.05 km) and ours (5 km),
400 along with the smoothing we applied, we do not consider such a comparison meaningful.

401



402

403

404

Figure 8: (a–d) Difference in gridded depth of four isochrones mapped by this study from M15. (e–h) Same as above, except for the age at normalized depths.

405

5 Discussion

406

407

408

409

410

411

412

413

Much has been written about the potential value of – and the challenge of producing – large-scale ice-sheet radiostratigraphy datasets (e.g., Karlsson et al., 2013; Sime et al., 2014; Moqadam and Eisen, in review; Bingham et al., in review). As with all methods of observation or data analysis, future improvements therein are almost inevitable. However, at some point the unique capabilities of the system in question – whether they be resolution, speed, accuracy or some other characteristic – must be locked so that the observation or analysis of interest can be made. Both M15 and this study assessed several methods for accelerating tracing but – critically – eventually paused that assessment and shifted gears to the actual production of an ice-sheet radiostratigraphy. This production stage revealed several challenges associated with QC’ing, dating and normalizing a large-scale radiostratigraphy (e.g., Fig. 2; §3), but several subsequent related studies have focused mostly

414 on designing or assessing alternative methods for tracing or slope estimation (e.g., Panton, 2014; Delf et al., 2020), with
415 relatively few that consider dating reflections not observed at ice cores (Cavitt et al., 2021). Further, it is now well established
416 that it is relatively easy to trace many reflections in any one of the two dozen or so high-quality KU/CRISIS VHF radargrams
417 that cross the northern GrIS (Fig. 1b; e.g., Panton, 2004; Xiong et al., 2018). It is much harder to trace discontinuous reflections
418 within ~300 km of the ice margin, harder still within ~100 km, and even harder to confidently propagate ages from interior ice
419 cores toward the periphery.

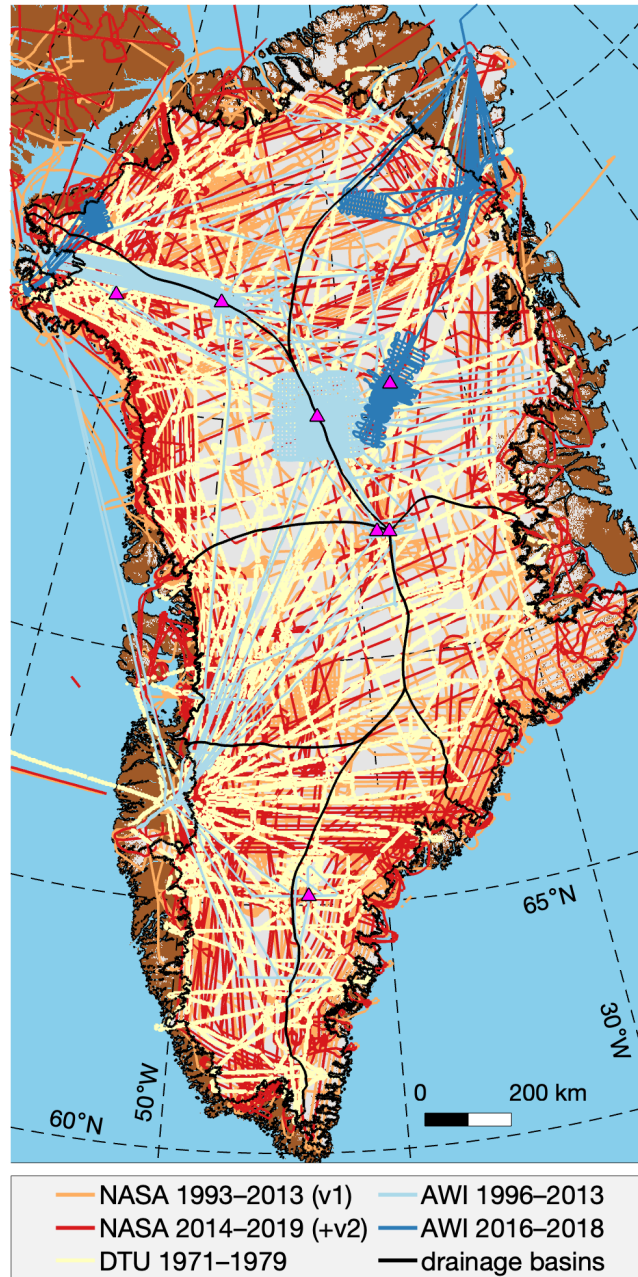
420 Despite the clear advantage of scale provided by our approach to mapping radiostratigraphy, our current approach
421 possesses some limitations that could be addressed in future versions. A primary limitation is that – while the GrIS
422 radiostratigraphy v2 dataset depends critically on the spatial relationships between segments and the matches between their
423 traced reflections – it is not a modern relational database through which updates to any individual element propagate
424 automatically. Instead, it is a series of static datasets developed in sequence (concatenated radargram segments, traced
425 reflections, inter-segment reflection matches, reflection ages, and gridded depths/ages). In other words, if an error in tracing
426 any reflection is identified and adjusted, then any matches between that reflection and others must be manually re-verified and
427 the dating and gridding procedures would need to be re-run. A second but more tractable challenge is the dynamic display of
428 intersecting segments and associated traced reflections on 2-D radargrams, which would clarify how far to attempt to trace
429 reflections to maximize the potential for matching them between segments. Alternatively, such inter-segment relationships can
430 sometimes be obvious in three-dimensional (*3-D*) perspectives of intersecting radargrams and their traced reflections (e.g.,
431 Franke et al., 2023). However, we experimented extensively with such 3-D perspectives in both MATLAB™ and PyVista
432 (Sullivan et al., 2019) and found that modifying or matching mapped radiostratigraphy remains cumbersome in 3-D when
433 evaluating many segment intersections (11 196 in this study).

434 To address the challenge of extracting useful geophysical information from large data volumes, machine learning (*ML*)
435 methods have been increasingly deployed in many fields of Earth science. The constellation of ML methods clearly possesses
436 great potential for accelerating the tracing of radiostratigraphy, but they face several broad challenges before they can be
437 widely adopted (Moqadam and Eisen, in review; Moqadam et al., in review; Peng et al., 2024). First, most ML methods use
438 supervised learning, which typically requires large training datasets. In this case, such datasets would be radargrams that have
439 been traced exhaustively, i.e., those that possess few or no false negatives. However, all presently available large-scale
440 radiostratigraphy datasets – including the one presented in this study – left innumerable observed reflections untraced. These
441 reflections were typically less distinct, less bright or shorter – and so they were deprioritized in our workflow (§3.1). We
442 suggest that suitable ML methods for tracing radiostratigraphy are those that can better tolerate inevitable and copious false
443 negatives, perhaps by being trained on synthetic radargrams or using ARESELP-generated predictions (Culberg and Schroeder,
444 2021; Jebeli et al., 2023). A second and related issue is the question of which reflections should be traced. An answer with a
445 future ML application in mind could simply be “all of them”, but perhaps a more realistic and readily achievable answer is
446 “those that models seek to match”. In the latter more restrained scenario, which was implicit in our tracing strategy, we may
447 consider both which observed reflections are clearly distinct from others *and* those which models seek to reproduce to better

448 resolve ice-sheet history, i.e., typically those associated with or close to major climate transitions (e.g., Born and Robinson,
449 2021; Sutter et al., 2021). However, how to enable ML to perform a similar prioritization remains unclear. Third, as emphasized
450 by Delf et al. (2020) and applicable to all automated methods for tracing radiostratigraphy, improving our ability to automate
451 the matching of reflections across discontinuities – whether due to an acquisition malfunction or observation limitation such
452 as steep reflection slopes – remains an outstanding challenge, and it is not yet clear how ML can accelerate this process.

453 As originally conceived, this dataset (GrIS radiostratigraphy v2) would have included additional VHF airborne radar-
454 sounding data collected primarily by institutions besides the US (Fig. 9). These include the first such data collected across the
455 GrIS during the 1970's by a Danish–British–American consortium that was recently digitized by Karlsson et al. (2024), surveys
456 of the northern and central GrIS mostly from the 1990s led by AWI (e.g., Nixdorf and Göktas, 2001), and more recent AWI
457 surveys using newer CReSIS-built radar systems (e.g., Kjær et al., 2018; Franke et al., 2022, 2023; Jansen et al., 2024).
458 Including these data was ultimately beyond the scope of this study but remains possible and could help fill remaining gaps in
459 coverage – especially in the northern half of the GrIS. A potential challenge in incorporating these data would be their different
460 center frequencies and bandwidths, which result in different patterns of interfering reflections – particularly in reflection-rich
461 Holocene ice. For the newer AWI data (2016–present), this challenge is due to the higher center frequency and wider bandwidth
462 of the system used that would typically result in more reflections being distinguishable, whereas for the other mostly older
463 data the challenge is reversed. Because we found that certain distinct reflections could be matched between KU/CReSIS
464 systems from 1993 all the way through to 2019, there is reason for cautious optimism in merging such disparate datasets.
465 Further, there is precedent in Antarctica for similar multi-system reconciliation of radiostratigraphy (Bodart et al., 2021; Winter
466 et al., 2017; Cavitte et al., 2021; Franke et al., 2025), and the bandwidth of some of the older AWI data (short chirp mode) or
467 the newer AWI data operated in narrowband mode is comparable to most of the radar systems considered here. For the older
468 1970's data, their greater geolocation uncertainty may also present an additional challenge in matching reflections with those
469 from newer systems.

470



471

472 **Figure 9:** Airborne radar-sounding surveys collected across the GrIS led by various institutions that could be included in future versions of
 473 a GrIS radiostratigraphy (AWI: Franke et al., 2023; O. Eisen and D. Steinhage, pers. comm., 2020; DTU: Karlsson et al., 2024), as compared
 474 to that collected primarily by NASA/KU/CRISIS between 1993–2019.

475

476

477

Given its improved spatial coverage, more robust QC and more accessible data formatting (§6), we expect that this second version of the GrIS-wide radiostratigraphy will help fully realize part of the original purpose for generation of the M15 dataset – to “[provide] a new constraint on the dynamics and history of the [GrIS]” – but also to expand the range of potential

478 applications for such a dataset. The v2 gridded products can be used to evaluate the modern age structure of initialized ice-
 479 sheet models to validate their overall climate sensitivity and various model parameterizations, especially past accumulation
 480 rates (e.g., Born and Robinson, 2021; Sutter et al., 2021; Rieckh et al., 2024). Following the methods introduced by those
 481 recent studies, the capability to record and advect ice age non-diffusively using a Lagrangian approximation was also
 482 introduced recently (in v2.1) to the widely used Parallel Ice Sheet Model (<https://www.pism.io/>; e.g., Aschwanden et al., 2019),
 483 which expands the potential user base for model evaluation of the age structure of the GrIS. At coarser scales, the gridded
 484 datasets can be more reliably used to distinguish between Holocene and pre-Holocene ice, which is valuable for radiometric
 485 studies of radargrams (e.g., MacGregor et al., 2015b; Chu et al., 2018) and interpretation of bulk rheology (e.g., MacGregor
 486 et al., 2016a). Finally, the along-track traced reflections can be used to rapidly identify anomalous structures within the ice
 487 sheet that can be either diagnosed simply using steady-state models (e.g., MacGregor et al., 2016b) or targeted for more detailed
 488 diagnosis using structural analyses (e.g., Franke et al., 2022).

489 6 Code and data availability

490 The MATLAB™ GUIs, functions and scripts and Jupyter notebooks used to perform the analysis and generate the figures in
 491 this manuscript are available at <https://doi.org/10.5281/zenodo.14183061> (MacGregor, 2024a). Most of the analysis was
 492 performed using functions built-in to several versions of MATLAB™ (R2022a to R2024b) with its associated Image
 493 Processing, Mapping, Statistics and Wavelet toolboxes. Python v3.12, various standard packages, and GStatSim were used to
 494 krigé the dataset (MacKie et al., 2023).

495 The datasets resulting from this study, which together constitute version 2 of Greenland’s deep radiostratigraphy, are
 496 available at <https://doi.org/10.5281/zenodo.15132763> (MacGregor et al., 2025) and may also be later made available through
 497 the National Snow and Ice Data Center, where further dataset-specific documentation will be provided. Table 3 describes the
 498 format of the HDF-5-compatible MATLAB™ (v7.3 .mat) files that contain each campaign’s traced reflections for each
 499 segment. Table 4 describes the format of the GeoPackage (.gpkg) files that contain the depths of each segment’s traced
 500 reflections, as we anticipate that these will be the most widely used reflection properties. These GeoPackage files are a more
 501 openly accessible version of the MATLAB files, but include many fewer reflection properties due to limitations of the format.
 502 Reflection ages and age uncertainties are preserved in each GeoPackage file’s metadata. Table 5 describes the format of the
 503 NetCDF (.nc) file that contains the gridded (5 km horizontal resolution) isochrone depths and ages at normalized depths (§3.3,
 504 4). For brevity, in these three tables we describe only the key variables and not all preserved metadata or other attributes.

505
 506 **Table 3:** Format of the “segment” structure in the MATLAB file for each campaign that contains the traced reflections at the radargram
 507 resolution.

| Variable | Description | Units |
|----------|-------------|-------|
|----------|-------------|-------|

| | | |
|-------------------------|---|-----|
| name | Name of segment, including concatenated frames used | N/A |
| dist | Along-track distance, calculated using great circles and the WGS84 ellipsoid | m |
| lat | Latitude | ° |
| lon | Longitude | ° |
| num_layer | Number of traced reflections | N/A |
| num_trace | Number of traces in the concatenated segment | N/A |
| thick | Ice thickness | m |
| time | GPS measurement time since 0000-01-01 | s |
| x | Projected x-coordinate, EPSG:3413 | m |
| y | Projected y-coordinate, EPSG:3413 | m |
| firm_corr | Modeled firn correction | m |
| stratigraphy | Structure with number of objects equal to num_layer that includes fields for each reflection property | N/A |
| stratigraphy.age | Reflection age | ka |
| stratigraphy.age_uncert | Uncertainty in reflection age | ka |
| stratigraphy.depth | Depth below ice surface to reflection (not corrected for firn) | m |
| stratigraphy.elev | Reflection elevation relative to WGS84 ellipsoid | m |
| stratigraphy.int | Reflection relative echo intensity (single sample, not window-integrated) | dB |
| stratigraphy.twtt | Englacial traveltime to reflection | s |

508

509 **Table 4:** Format of GeoPackage files for each concatenated segment that contains the traced reflections at the radargram resolution.

| Variable | Description | Units |
|----------|--|-------|
| geometry | Projected x- and y- coordinates, EPSG:3413 | m |
| thick | Ice thickness | m |
| time | GPS measurement time since 0000-01-01 | s |

depth_XY.Z Depth below ice surface (not m
corrected for firn) to reflection whose
age is X ka. If undated, the age is
given as U. If more than one
reflection is dated to that age (or
undated), then the variable name is
hyphenated with -0, -1 and so forth.

510

511 **Table 5:** Format of NetCDF file that contains the gridded isochrone depths and ages at normalized depths.

| Variable | Description | Units |
|------------|--|-------|
| x | Projected x-coordinate, EPSG:3413 | m |
| y | Projected y-coordinate, EPSG:3413 | m |
| age_iso | Ages of synthetic isochrones whose depth was gridded (depth, depthstd) | ka |
| age | Age at normalized depth | ka |
| agestd | Total uncertainty in age at normalized depth | ka |
| depth_norm | Thickness-normalized depths whose age was gridded (age, agestd) | % |
| depth | Isochrone depth | m |
| depthstd | Total uncertainty in isochrone depth | m |

512

7 Conclusions

513

514

515

516

517

518

519

520

521

522

523

524

We produced a second version of a dated radiostratigraphic dataset covering a substantial portion (up to 65%) of the GrIS using a non-repeating subset of available NASA/NSF radargrams. While far from comprehensive, as innumerable minor reflections were left untraced – let alone dated – this dataset represents an improved and potentially large-scale constraint on models of the flow of the GrIS and their sensitivity to past climate change. The inferred basic age structure of the GrIS is not significantly changed from that which M15 first described, but its development was simplified, and the resulting dataset has substantially fewer tracing errors, is more self-consistent and is expected to be more robust for future modeling efforts. This version of the dataset continues to indicate that the oldest ice in the Greenland is likely in northern central GrIS, that the ice sheet is significantly older in northeastern and far northern Greenland, and that the radiostratigraphy and age structure of the GrIS south of 65°N remains challenging to map using presently available data and techniques. Finally, we modernized and further generalized the tools used to generate this radiostratigraphy – as compared to the previous version of the dataset – and expect that they could be used to either improve upon this dataset in the future for the GrIS or to accelerate Antarctic-wide mapping of radiostratigraphy.

525 **Author contribution.** JAM, MAF and AA secured funding for this study. JAM performed most of the tracing and QC, led the
526 subsequent analysis, and drafted the manuscript. MAF aided in the analysis. JDP and JL processed the radar data. JPH traced
527 some of the radar data. All authors reviewed and edited the manuscript.

528 **Video supplement.** Movie S1 is available at both <https://doi.org/10.5281/zenodo.14531649> (MacGregor, 2024b) and also on
529 YouTube (<https://www.youtube.com/watch?v=eB0IVrQ0Awo>). Because of its size (3.3 GB), it is provided separate from the
530 dataset itself. This movie shows all 496 traced segments in chronological sequence, corrected for surface elevation as in Fig.
531 3e. A 50-km portion of each radargram is shown in each frame, which is translated by 20 km between each frame and is
532 recorded at 5 frames per second. Traced and dated reflections are shown in every other frame to enable visual evaluation of
533 the traced radiostratigraphy. An inset map of Greenland shows all traced segments, highlighting the current segment in blue
534 and the current frame in red. The color range of the displayed radargram is rescaled for each frame to the mean \pm two standard
535 deviations of the radargram amplitudes within that frame.

536 **Competing interests.** None declared.

537 **Acknowledgments.** We thank the NASA Cryospheric Sciences program for funding this study (solicitation
538 #NNH20ZDA001N) and the innumerable individuals who supported and performed the airborne surveys, ice-core drilling and
539 related work that ultimately made this study possible. We thank O. Eisen, N. B. Karlsson, E. J. MacKie, T. Rieckh and D.
540 Steinhage for valuable discussions.

541 **References**

- 542 Aschwanden, A., Fahnestock, M. A., Truffer, M., Brinkerhoff, D. J., Hock, R., Khroulev, C., Mottram, R., and Khan, S. A.:
543 Contribution of the Greenland Ice Sheet to sea level over the next millennium, *Sci. Adv.*, 5, eaav9396, [https://doi.org/](https://doi.org/10.1126/sciadv.aav9396)
544 [10.1126/sciadv.aav9396](https://doi.org/10.1126/sciadv.aav9396), 2019.
- 545 Aschwanden, A., Bartholomaus, T. C., Brinkerhoff, D. J., Truffer, M.: Brief communication: A roadmap towards credible
546 projections of ice sheet contribution to sea level, *The Cryosphere*, 15, 5705–5715, <https://doi.org/10.5194/tc-15-5705-2021>,
547 2021.
- 548 Aschwanden, A. and Brinkerhoff, D. J.: Calibrated Mass Loss Predictions for the Greenland Ice Sheet, *Geophys. Res. Lett.*,
549 49, <https://doi.org/10.1029/2022gl099058>, 2022.
- 550 Bingham, R. G., Bodart, J. A., Cavitte, M. G. P., Chung, A., Sanderson, R. J., Sutter, J. C. R., Eisen, O., Karlsson, N. B.,
551 MacGregor, J. A., Ross, N., Young, D. A., Ashmore, D. W., Born, A., Chu, W., Cui, X., Drews, R., Franke, S., Goel, V.,
552 Goodge, J. W., Henry, A. C. J., Hermant, A., Hills, B. H., Holschuh, N., Koutnik, M. R., Leysinger Vieli, G. J.-M. C.,

553 Mackie, E. J., Mantelli, E., Martín, C., Ng, F. S. L., Oraschewski, F. M., Napoleoni, F., Parrenin, F., Popov, S. V., Rieckh,
554 T., Schlegel, R., Schroeder, D. M., Siegert, M. J., Tang, X., Teisberg, T. O., Winter, K., Yan, S., Davis, H., Dow, C. F.,
555 Fudge, T. J., Jordan, T. A., Kulesa, B., Matsuoka, K., Nyqvist, C. J., Rahmemonfar, M., Siegfried, M. R., Singh, S.,
556 Višnjević, V., Zamora, R., and Zühr, A.: Review Article: Antarctica's internal architecture: Towards a radiostratigraphically-
557 informed age–depth model of the Antarctic ice sheets, *EGU*sphere [preprint], <https://doi.org/10.5194/egusphere-2024-2593>,
558 2024.

559 Bodart, J. A., Bingham, R. G., Ashmore, D. W., Karlsson, N. B., Hein, A. S., and Vaughan, D. G.: Age-Depth Stratigraphy of
560 Pine Island Glacier Inferred From Airborne Radar and Ice-Core Chronology, *J. Geophys. Res.: Earth Surf.*, 126,
561 <https://doi.org/10.1029/2020jg005927>, 2021.

562 Bons, P. D., Jansen, D., Mundel, F., Bauer, C. C., Binder, T., Eisen, O., Jessell, M. W., Llorens, M.-G., Steinbach, F.,
563 Steinhage, D. and Weikusat, I.: Converging flow and anisotropy cause large-scale folding in Greenland's ice sheet, *Nature*
564 *Commun.*, 7, 1–6, <https://doi.org/10.1038/ncomms11427>, 2016.

565 Born, A. and Robinson, A.: Modeling the Greenland englacial stratigraphy, *The Cryosphere*, 15, 4539–4556,
566 <https://doi.org/10.5194/tc-2020-355>, 2021.

567 Castelletti, D., Schroeder, D. M., Mantelli, E., and Hilger, A.: Layer optimized SAR processing and slope estimation in radar
568 sounder data, *J. Glaciol.*, 65, 983–988, <https://doi.org/10.1017/jog.2019.72>, 2019.

569 Cavitte, M. G. P., Young, D. A., Mulvaney, R., Ritz, C., Greenbaum, J. S., Ng, G., Kempf, S. D., Quartini, E., Muldoon, G.
570 R., Paden, J., Frezzotti, M., Roberts, J. L., Tozer, C. R., Schroeder, D. M., and Blankenship, D. D.: A detailed
571 radiostratigraphic data set for the central East Antarctic Plateau spanning from the Holocene to the mid-Pleistocene, *Earth*
572 *Syst. Sci. Data*, 13, 4759–4777, <https://doi.org/10.5194/essd-13-4759-2021>, 2021.

573 Chu, W., Schroeder, D. M., Seroussi, H., Creyts, T. T., and Bell, R. E.: Complex Basal Thermal Transition Near the Onset of
574 Petermann Glacier, Greenland, *J. Geophys. Res.: Earth Surf.*, 123, 985–995, <https://doi.org/10.1029/2017jg004561>, 2018.

575 Cooper, M. A., Jordan, T. M., Schroeder, D. M., Siegert, M. J., Williams, C. N., and Bamber, J. L.: Subglacial roughness of
576 the Greenland Ice Sheet: relationship with contemporary ice velocity and geology, *The Cryosphere*, 13, 3093–3115,
577 <https://doi.org/10.5194/tc-13-3093-2019>, 2019.

578 Csatho, B. M., Schenk, A. F., Veen, C. J. van der, Babonis, G., Duncan, K., Rezvanbehbahani, S., Broeke, M. R. van den,
579 Simonsen, S. B., Nagarajan, S., and Angelen, J. H. van: Laser altimetry reveals complex pattern of Greenland Ice Sheet
580 dynamics, *Proc. Natl. Acad. Sci.*, 111, 18478–18483, <https://doi.org/10.1073/pnas.1411680112>, 2014.

581 Culberg, R. and Schroeder, D. M.: Simulations of Englacial Radiostratigraphy from ICE Core Measurements, 2021 IEEE Int.
582 *Geosci. Remote Sens. Symp. IGARSS*, 2943–2946, <https://doi.org/10.1109/igarss47720.2021.9553760>, 2021.

583 Dahl-Jensen, D., Albert, M. R., Aldahan, A., Azuma, N., Balslev-Clausen, D., Baumgartner, M., Berggren, A. M., Bigler, M.,
584 Binder, T., Blunier, T., Bourgeois, J. C., Brook, E. J., Buchardt, S. L., Buizert, C., Capron, E., Chappellaz, J., Chung, J.,
585 Clausen, H. B., Cvijanovic, I., Davies, S. M., Ditlevsen, P., Eicher, O., Fischer, H., Fisher, D. A., Fleet, L. G., Gfeller, G.,
586 Gkinis, V., Gogineni, S. P., Goto-Azuma, K., Grinsted, A., Gudlaugsdottir, H., Guillevic, M., Hansen, S. B., Hansson, M.

587 E., Hirabayashi, M., Hong, S. M., Hur, S. D., Huybrechts, P., Hvidberg, C., Iizuka, Y., Jenk, T., Johnsen, S., Jones, T. R.,
588 Jouzel, J., Karlsson, N. B., Kawamura, K., Keegan, K., Kettner, E., Kipfstuhl, S., Kjær, H. A., Koutnik, M. R., Kuramoto,
589 T., Köhler, P., Laepple, T., Landais, A., Langen, P. L., Larsen, L. B., Leuenberger, D., Leuenberger, M., Leuschen, C. J.,
590 Li, J., Lipenkov, V. Y., Martinerie, P., Maselli, O. J., Masson-Delmotte, V., McConnell, J. R., Millar, D. H. M., Mini, O.,
591 Miyamoto, A., Montagnat-Rentier, M., Mulvaney, R., Muscheler, R., Orsi, A. J., Paden, J. D., Panton, C., Pattyn, F., Petit,
592 J.-R., Pol, K., Popp, T. J., Possnert, G., Prié, F., Prokopiou, M., Quiquet, A., Rasmussen, S. O., Raynaud, D., Ren, J. W.,
593 Reutenauer, C., Ritz, C., Röckmann, T., Rosen, J. L., Rubino, M., Rybak, O., Samyn, D., Sapart, C. J., Schilt, A., Schmidt,
594 A. M. Z., Schwander, J., Schüpbach, S., Seierstad, I., Severinghaus, J. P., Sheldon, S., Simonsen, S. B., Sjolte, J., Solgaard,
595 A. M., Sowers, T. A., Sperlich, P., Steen-Larsen, H. C., Steffen, K., Steffensen, J. P., Steinhage, D., Stocker, T. F., Stowasser,
596 C., Sturevik, A. S., Sturges, W. T., Sveinbjornsdottir, A. E., Svensson, A. M., Tison, J. L., Uetake, J., Vallelonga, P., van de
597 Wal, R. S. W., van der Wel, G., Vaughn, B. H., Vinther, B. M., Waddington, E. D., Wegner, A., Weikusat, I., White, J.,
598 Wilhelms, F., Winstrup, M., Witrant, E., Wolff, E. W., Xiao, C. D. and Zheng, J.: Eemian interglacial reconstructed from a
599 Greenland folded ice core, *Nature*, 493, 489–494, <https://doi.org/10.1038/nature11789>, 2013.

600 Das, I., Bell, R. E., Scambos, T. A., Wolovick, M., Creyts, T. T., Studinger, M., Frearson, N., Nicolas, J. P., Lenaerts, J. T.
601 M., and Broeke, M. R. van den: Influence of persistent wind scour on the surface mass balance of Antarctica, *Nat. Geosci.*,
602 6, 367–371, <https://doi.org/10.1038/ngeo1766>, 2013.

603 Delf, R., Schroeder, D. M., Curtis, A., Giannopoulos, A., and Bingham, R. G.: A comparison of automated approaches to
604 extracting englacial-layer geometry from radar data across ice sheets, *Ann. Glaciol.*, 61, 234–241,
605 <https://doi.org/10.1017/aog.2020.42>, 2020.

606 Dow, C. F., Karlsson, N. B. and Werder, M. A.: Limited Impact of Subglacial Supercooling Freeze-on for Greenland Ice Sheet
607 Stratigraphy, *Geophys. Res. Lett.*, 45, 1481–1489, <https://doi.org/10.1002/2017gl076251>, 2018.

608 Franke, S., Bons, P. D., Westhoff, J., Weikusat, I., Binder, T., Streng, K., Steinhage, D., Helm, V., Eisen, O., Paden, J. D.,
609 Eagles, G., and Jansen, D.: Holocene ice-stream shutdown and drainage basin reconfiguration in northeast Greenland, *Nat.*
610 *Geosci.*, 15, 995–1001, <https://doi.org/10.1038/s41561-022-01082-2>, 2022.

611 Franke, S., Bons, P. D., Streng, K., Mundel, F., Binder, T., Weikusat, I., Bauer, C. C., Paden, J. D., Dörr, N., Helm, V.,
612 Steinhage, D., Eisen, O., and Jansen, D.: Three-dimensional topology dataset of folded radar stratigraphy in northern
613 Greenland, *Sci. Data*, 10, 525, <https://doi.org/10.1038/s41597-023-02339-0>, 2023.

614 Franke, S., Steinhage, D., Helm, V., Zuhr, A. M., Bodart, J. A., Eisen, O., and Bons, P.: Age-depth distribution in western
615 Dronning Maud Land, East Antarctica, and Antarctic-wide comparisons of internal reflection horizons, *The Cryosphere*, 19,
616 1153–1180, <https://doi.org/10.5194/tc-19-1153-2025>, 2025.

617 Goelzer, H., Nowicki, S., Edwards, T., Beckley, M., Abe-Ouchi, A., Aschwanden, A., Calov, R., Gagliardini, O., Gillet-
618 Chaulet, F., Gollledge, N. R., Gregory, J., Greve, R., Humbert, A., Huybrechts, P., Kennedy, J. H., Larour, E., Lipscomb,
619 W. H., Lec'h, S. L., Lee, V., Morlighem, M., Pattyn, F., Payne, A. J., Rodehacke, C., Rückamp, M., Saito, F., Schlegel, N.,
620 Seroussi, H., Shepherd, A., Sun, S., Wal, R. van de, and Ziemen, F. A.: Design and results of the ice sheet model initialisation

621 experiments initMIP-Greenland: an ISMIP6 intercomparison, *The Cryosphere*, 12, 1433–1460, [https://doi.org/10.5194/tc-](https://doi.org/10.5194/tc-12-1433-2018)
622 12-1433-2018, 2018.

623 Goelzer, H., Nowicki, S., Payne, A., Larour, E., Seroussi, H., Lipscomb, W. H., Gregory, J., Abe-Ouchi, A., Shepherd, A.,
624 Simon, E., Agosta, C., Alexander, P., Aschwanden, A., Barthel, A., Calov, R., Chambers, C., Choi, Y., Cuzzzone, J., Dumas,
625 C., Edwards, T., Felikson, D., Fettweis, X., Golledge, N. R., Greve, R., Humbert, A., Huybrechts, P., Le clec’h, S., Lee, V.,
626 Leguy, G., Little, C., Lowry, D. P., Morlighem, M., Nias, I., Quiquet, A., Rückamp, M., Schlegel, N.-J., Slater, D. A., Smith,
627 R. S., Straneo, F., Tarasov, L., van de Wal, R. and van den Broeke, M.: The future sea-level contribution of the Greenland
628 ice sheet: a multi-model ensemble study of ISMIP6, *The Cryosphere*, 14, 3071–3096, [https://doi.org/10.5194/tc-14-3071-](https://doi.org/10.5194/tc-14-3071-2020)
629 2020, 2020.

630 Hindmarsh, R. C. A., Leysinger-Vieli, G. J. -M. C., Raymond, M. J., and Gudmundsson, G. H.: Draping or overriding: The
631 effect of horizontal stress gradients on internal layer architecture in ice sheets, *J. Geophys. Res.*, 111, F02018,
632 <https://doi.org/10.1029/2005jf000309>, 2006.

633 Howat, I. M., Negrete, A. and Smith, B. E.: The Greenland Ice Mapping Project (GIMP) land classification and surface
634 elevation data sets, *The Cryosphere*, 8, 1509–1518, <https://doi.org/10.5194/tc-8-1509-2014>, 2014.

635 Jansen, D., Franke, S., Bauer, C. C., Binder, T., Dahl-Jensen, D., Eichler, J., Eisen, O., Hu, Y., Kerch, J., Llorens, M.-G.,
636 Miller, H., Neckel, N., Paden, J., Riese, T. de, Sachau, T., Stoll, N., Weikusat, I., Wilhelms, F., Zhang, Y., and Bons, P. D.:
637 Shear margins in upper half of Northeast Greenland Ice Stream were established two millennia ago, *Nat. Commun.*, 15,
638 1193, <https://doi.org/10.1038/s41467-024-45021-8>, 2024.

639 Jebeli, A., Tama, B. A., Janeja, V. P., Holschuh, N., Jensen, C., Morlighem, M., MacGregor, J. A., and Fahnestock, M. A.:
640 TSSA: Two-Step Semi-Supervised Annotation for Radargrams on the Greenland Ice Sheet, *IGARSS 2023 - 2023 IEEE Int.*
641 *Geosci. Remote Sens. Symp.*, 00, 56–59, <https://doi.org/10.1109/igarss52108.2023.10282880>, 2023.

642 Karlsson, N. B., Dahl-Jensen, D., Gogineni, S. P., and Paden, J. D.: Tracing the depth of the Holocene ice in North Greenland
643 from radio-echo sounding data, *Ann. Glaciol.*, 54, 44–50, <https://doi.org/10.3189/2013aog64a057>, 2013.

644 Karlsson, N. B., Schroeder, D. M., Sørensen, L. S., Chu, W., Dall, J., Andersen, N. H., Dobson, R., Mackie, E. J., Köhn, S. J.,
645 Steinmetz, J. E., Tarzona, A. S., Teisberg, T. O., and Skou, N.: A newly digitized ice-penetrating radar data set acquired
646 over the Greenland ice sheet in 1971–1979, *Earth Syst. Sci. Data*, 16, 3333–3344, [https://doi.org/10.5194/essd-16-3333-](https://doi.org/10.5194/essd-16-3333-2024)
647 2024, 2024.

648 Kjør, K. H., Larsen, N. K., Binder, T., Bjørk, A. A., Eisen, O., Fahnestock, M. A., Funder, S., Garde, A. A., Haack, H., Helm,
649 V., Houmark-Nielsen, M., Kjeldsen, K. K., Khan, S. A., Machguth, H., McDonald, I., Morlighem, M., Mougnot, J., Paden,
650 J. D., Waight, T. E., Weikusat, C., Willerslev, E. and MacGregor, J. A.: A large impact crater beneath Hiawatha Glacier in
651 northwest Greenland, *Sci. Adv.*, 4(11), <https://doi.org/10.1126/sciadv.aar8173>, 2018.

652 Krabill, W., Abdalati, W., Frederick, E., Manizade, S., Martin, C., Sonntag, J., Swift, R., Thomas, R., Wright, W., and Yungel,
653 J.: Greenland Ice Sheet: High-Elevation Balance and Peripheral Thinning, *Science*, 289, 428–430,
654 <https://doi.org/10.1126/science.289.5478.428>, 2000.

655 Leysinger-Vieli, G. J. M. C., Martin, C., Hindmarsh, R. C. A. and Lüthi, M. P.: Basal freeze-on generates complex ice-sheet
656 stratigraphy, *Nature Commun.*, 9, <https://doi.org/10.1038/s41467-018-07083-3>, 2018.

657 MacGregor, J. A., Fahnestock, M. A., Catania, G. A., Paden, J. D., Gogineni, S. P., Young, S. K., Rybarski, S. C., Mabrey,
658 A. N., Wagman, B. M. and Morlighem, M.: Radiostratigraphy and age structure of the Greenland Ice Sheet, *J. Geophys.*
659 *Res. Earth Surf.*, 120(2), 212–241, <https://doi.org/10.1002/2014jgf003215>, 2015a.

660 MacGregor, J. A., Li, J., Paden, J. D., Catania, G. A., Clow, G. D., Fahnestock, M. A., Gogineni, S. P., Grimm, R., Morlighem,
661 M., Nandi, S., Seroussi, H. and Stillman, D. E.: Radar attenuation and temperature within the Greenland Ice Sheet, *J.*
662 *Geophys. Res.: Earth Surf.*, 120(6), 983–1008, <https://doi.org/10.1002/2014jgf003418>, 2015b.

663 MacGregor, J. A., Colgan, W. T., Fahnestock, M. A., Morlighem, M., Catania, G. A., Paden, J. D., and Gogineni, S. P.:
664 Holocene deceleration of the Greenland Ice Sheet, *Science*, 351, 590–593, <https://doi.org/10.1126/science.aab1702>, 2016a.

665 MacGregor, J. A., Fahnestock, M. A., Catania, G. A., Aschwanden, A., Clow, G. D., Colgan, W. T., Gogineni, S. P.,
666 Morlighem, M., Nowicki, S. M. J., Paden, J. D., Price, S. F. and Seroussi, H.: A synthesis of the basal thermal state of the
667 Greenland Ice Sheet, *J. Geophys. Res.: Earth Surf.*, 121(7), 1328–1350, <https://doi.org/10.1002/2015jgf003803>, 2016b.

668 MacGregor, J. A., Fahnestock, M. A., Colgan, W. T., Larsen, N. K., Kjeldsen, K. K., and Welker, J. M.: The age of surface-
669 exposed ice along the northern margin of the Greenland Ice Sheet, *J. Glaciol.*, 66, 667–684,
670 <https://doi.org/10.1017/jog.2020.62>, 2020.

671 MacGregor, J. A., Boisvert, L. N., Medley, B., Petty, A. A., Harbeck, J. P., Bell, R. E., Blair, J. B., Blanchard-Wrigglesworth,
672 E., Buckley, E. M., Christoffersen, M. S., Cochran, J. R., Csathó, B. M., De Marco, E. L., Dominguez, R. T., Fahnestock,
673 M. A., Farrell, S. L., Gogineni, S. P., Greenbaum, J. S., Hansen, C. M., Hofton, M. A., Holt, J. W., Jezek, K. C., Koenig, L.
674 S., Kurtz, N. T., Kwok, R., Larsen, C. F., Leuschen, C. J., Locke, C.D., Manizade, S. S., Martin, S., Neumann, T. A.,
675 Nowicki, S. M. J., Paden, J. D., Richter-Menge, J. A., Rignot, E. J., Rodríguez-Morales, F., Siegfried, M. R., Smith, B. E.,
676 Sonntag, J. G., Studinger, M., Tinto, K. J., Truffer, M., Wagner, T. P., Woods, J. E., Young, D. A. and Yungel, J. K.: The
677 scientific legacy of NASA’s Operation IceBridge, *Rev. Geophys.*, 59, <https://doi.org/10.1029/2020RG000712>, 2021.

678 MacGregor, J. A., Chu, W., Colgan, W. T., Fahnestock, M. A., Felikson, D., Karlsson, N. B., Nowicki, S. M. J., and Studinger,
679 M.: GBaTSv2: a revised synthesis of the likely basal thermal state of the Greenland Ice Sheet, *The Cryosphere*, 16, 3033–
680 3049, <https://doi.org/10.5194/tc-16-3033-2022>, 2022.

681 MacGregor, J. A., Fahnestock, M. A., Paden, J. D., Li, J., Harbeck, J. P., and Aschwanden, A.: Dataset for: A revised and
682 expanded deep radiostratigraphy of the Greenland Ice Sheet from airborne radar sounding surveys between 1993–2019,
683 *Zenodo*, <https://doi.org/10.5281/zenodo.15132763>, 2025.

684 MacGregor, J. A.: joemacgregor/pickgui: Version 2.0.1, Submission version of PICKGUI/FENCEGUI/etc for v2 of Greenland
685 radiostratigraphy (v2.0.1). *Zenodo*, <https://doi.org/10.5281/zenodo.14183061>, 2024a.

686 MacGregor, J. A.: Supplementary Video (Movie S1) for Greenland radiostratigraphy v2 dataset (Version 1). *Zenodo*,
687 <https://doi.org/10.5281/zenodo.14531649>, 2024b.

688 MacKie, E. J., Field, M., Wang, L., Yin, Z., Schoedl, N., Hibbs, M., and Zhang, A.: GStatSim V1.0: a Python package for
689 geostatistical interpolation and conditional simulation, *Geosci. Model Dev.*, 16, 3765–3783, [https://doi.org/10.5194/gmd-](https://doi.org/10.5194/gmd-16-3765-2023)
690 16-3765-2023, 2023.

691 Medley, B., Neumann, T. A., Zwally, H. J., Smith, B. E., and Stevens, C. M.: Simulations of firn processes over the Greenland
692 and Antarctic ice sheets: 1980–2021, *The Cryosphere*, 16, 3971–4011, <https://doi.org/10.5194/tc-16-3971-2022>, 2022.

693 Mojtabavi, S., Wilhelms, F., Cook, E., Davies, S. M., Sinnl, G., Skov Jensen, M., Dahl-Jensen, D., Svensson, A., Vinther, B.
694 M., Kipfstuhl, S., Jones, G., Karlsson, N. B., Faria, S. H., Gkinis, V., Kjær, H. A., Erhardt, T., Berben, S. M. P., Nisancioglu,
695 K. H., Koldtoft, I., and Rasmussen, S. O.: A first chronology for the East Greenland Ice-core Project (EGRIP) over the
696 Holocene and last glacial termination, *Climate of the Past*, 16, 2359–2380, <https://doi.org/10.5194/cp-16-2359-2020>, 2020.

697 Moqadam, H., and Eisen, O.: Review article: Feature tracing in radio-echo sounding products of terrestrial ice sheets and
698 planetary bodies, *EGUsphere*, <https://doi.org/10.5194/egusphere-2024-1674>, in review.

699 Moqadam, H., Steinhage, D., Wilhelm, A., and Eisen, O.: Going deeper with deep learning: automatically tracing internal
700 reflection horizons in ice sheets, *Machine Learning and Computation*,
701 [https://d197for5662m48.cloudfront.net/documents/publicationstatus/229337/preprint_pdf/b283884d4a95faa94a832b33ce7](https://d197for5662m48.cloudfront.net/documents/publicationstatus/229337/preprint_pdf/b283884d4a95faa94a832b33ce7e72d9.pdf)
702 e72d9.pdf, in review.

703 Morlighem, M., Williams, C. N., Rignot, E. J., An, L., Arndt, J. E., Bamber, J. L., Catania, G. A., Chauché, N., Dowdeswell,
704 J. A., Dorschel, B., Fenty, I., Hogan, K., Howat, I. M., Hubbard, A. L., Jakobsson, M., Jordan, T. M., Kjeldsen, K. K.,
705 Millan, R., Mayer, L., Mouginot, J., Noël, B. P. Y., O’Cofaigh, C., Palmer, S. J., Rysgaard, S., Seroussi, H., Siegert, M. J.,
706 Slabon, P., Straneo, F., Broeke, M. R. van den, Weinrebe, W., Wood, M. and Zinglensen, K. B.: BedMachine v3: Complete
707 Bed Topography and Ocean Bathymetry Mapping of Greenland From Multibeam Echo Sounding Combined With Mass
708 Conservation, *Geophys. Res. Lett.*, 44, 11,051–11,061, <https://doi.org/10.1002/2017gl074954>, 2017.

709 Morlighem, M., Williams, C. N., Rignot, E. J., An, L., Arndt, J. E., Bamber, J. L., Catania, G. A., Chauché, N., Dowdeswell,
710 J. A., Dorschel, B., Fenty, I., Hogan, K., Howat, I. M., Hubbard, A. L., Jakobsson, M., Jordan, T. M., Kjeldsen, K. K.,
711 Millan, R., Mayer, L., Mouginot, J., Noël, B. P. Y., O’Cofaigh, C., Palmer, S. J., Rysgaard, S., Seroussi, H., Siegert, M. J.,
712 Slabon, P., Straneo, F., Broeke, M. R. van den, Weinrebe, W., Wood, M. and Zinglensen, K. B.: IceBridge BedMachine
713 Greenland, Version 5, NASA National Snow and Ice Data Center Distributed Active Archive Center,
714 <https://doi.org/10.5067/VLJ5YXKCNGXO>, 2021.

715 Mouginot, J., Rignot, E. J., Bjørk, A. A., Broeke, M. R. van den, Millan, R., Morlighem, M., Noel, B., Scheuchl, B., and Wood,
716 M.: Forty-six years of Greenland Ice Sheet mass balance from 1972 to 2018, *Proc. Natl. Acad. Sci.*, 116 (19) 9239–9244,
717 <https://doi.org/10.7280/d1mm37>, 2019.

718 Nixdorf, U. and Göktas, F.: Spatial depth distribution of the subglacial bed and internal layers in the ice around NGRIP,
719 Greenland, derived with airborne RES, *J. Appl. Geophys.*, 175–182, [https://doi.org/10.1016/S0926-9851\(01\)00062-3](https://doi.org/10.1016/S0926-9851(01)00062-3), 2001.

720 Otosaka, I. N., Shepherd, A., Ivins, E. R., Schlegel, N.-J., Amory, C., Broeke, M. R. van den, Horwath, M., Joughin, I., King,
721 M. D., Krinner, G., Nowicki, S., Payne, A. J., Rignot, E., Scambos, T., Simon, K. M., Smith, B. E., Sørensen, L. S.,

722 Velicogna, I., Whitehouse, P. L., A. G., Agosta, C., Ahlström, A. P., Blazquez, A., Colgan, W., Engdahl, M. E., Fettweis,
723 X., Forsberg, R., Gallée, H., Gardner, A., Gilbert, L., Gourmelen, N., Groh, A., Gunter, B. C., Harig, C., Helm, V., Khan,
724 S. A., Kittel, C., Konrad, H., Langen, P. L., Lecavalier, B. S., Liang, C.-C., Loomis, B. D., McMillan, M., Melini, D.,
725 Mernild, S. H., Mottram, R., Mouginit, J., Nilsson, J., Noël, B., Pattle, M. E., Peltier, W. R., Pie, N., Roca, M., Sasgen, I.,
726 Save, H. V., Seo, K.-W., Scheuchl, B., Schrama, E. J. O., Schröder, L., Simonsen, S. B., Slater, T., Spada, G., Sutterley, T.
727 C., Vishwakarma, B. D., Wessem, J. M. van, Wiese, D., Wal, W. van der, and Wouters, B.: Mass balance of the Greenland
728 and Antarctic ice sheets from 1992 to 2020, *Earth Syst. Sci. Data*, 15, 1597–1616, [https://doi.org/10.5194/essd-15-1597-](https://doi.org/10.5194/essd-15-1597-2023)
729 2023, 2023.

730 Nereson, N. A., Raymond, C. F., Waddington, E. D., and Jacobel, R. W.: Migration of the Siple Dome ice divide, West
731 Antarctica. *J. Glaciol.*, 44, 643–652, <https://doi.org/10.3189/s002214300000214>, 1998.

732 Parrenin, F., Hindmarsh, R. C. A., and Rémy, F.: Analytical solutions for the effect of topography, accumulation rate and
733 lateral flow divergence on isochrone layer geometry, *J. Glaciol.*, 52, 191–202,
734 <https://doi.org/10.3189/172756506781828728>, 2006.

735 Pantou, C.: Automated mapping of local layer slope and tracing of internal layers in radio echograms, *Ann. Glaciol.*, 55, 71–
736 77, <https://doi.org/10.3189/2014aog67a048>, 2014.

737 Pantou, C. and Karlsson, N. B.: Automated mapping of near bed radio-echo layer disruptions in the Greenland Ice Sheet, *Earth*
738 *Planet. Sci. Lett.*, 432(C), 323–331, <https://doi.org/10.1016/j.epsl.2015.10.024>, 2015.

739 Peng, C., Zheng, L., Liang, Q., Li, T., Wu, J., and Cheng, X.: ST-SOLOv2: Tracing Depth Hoar Layers in Antarctic Ice Sheet
740 from Airborne Radar Echograms with Deep Learning, *IEEE Trans. Geosci. Remote Sens.*,
741 <https://doi.org/10.1109/tgrs.2024.3480698>, 2024.

742 Rasmussen, S. O., Andersen, K. K., Svensson, A. M., Steffensen, J. P., Vinther, B. M., Clausen, H. B., Siggaard-Andersen,
743 M. -L., Johnsen, S. J., Larsen, L. B., Dahl-Jensen, D., Bigler, M., Röthlisberger, R., Fischer, H., Goto-Azuma, K., Hansson,
744 M. E., and Ruth, U.: A new Greenland ice core chronology for the last glacial termination, *J. Geophys. Res.: Atmos.*, 111,
745 D06102, <https://doi.org/10.1029/2005jd006079>, 2006.

746 Rieckh, T., Born, A., Robinson, A., Law, R., and Gülle, G.: Design and performance of ELSA v2.0: an isochronal model for
747 ice-sheet layer tracing, *Geosci. Model Dev.*, 17, 6987–7000, <https://doi.org/10.5194/gmd-17-6987-2024>, 2024.

748 Rodríguez-Morales, F., Byers, K., Crowe, R., Player, K., Hale, R. D., Arnold, E. J., Smith, L., Gifford, C. M., Braaten, D.,
749 Pantou, C., Gogineni, S., Leuschen, C. J., Paden, J. D., Li, J., Lewis, C. C., Panzer, B., Alvestegui, D. Gomez-García, and
750 Patel, A.: Advanced Multifrequency Radar Instrumentation for Polar Research, *IEEE Trans. Geosci. Remote Sens.*, 52,
751 2824–2842, <https://doi.org/10.1109/tgrs.2013.2266415>, 2014.

752 Seierstad, I. K., Abbott, P. M., Bigler, M., Blunier, T., Bourne, A. J., Brook, E., Buchardt, S. L., Buizert, C., Clausen, H. B.,
753 Cook, E., Dahl-Jensen, D., Davies, S. M., Guillevic, M., Johnsen, S. J., Pedersen, D. S., Popp, T. J., Rasmussen, S. O.,
754 Severinghaus, J. P., Svensson, A., and Vinther, B. M.: Consistently dated records from the Greenland GRIP, GISP2 and

755 NGRIP ice cores for the past 104 ka reveal regional millennial-scale $\delta^{18}\text{O}$ gradients with possible Heinrich event imprint,
756 *Quat. Sci. Rev.*, 106, 29–46, <https://doi.org/10.1016/j.quascirev.2014.10.032>, 2014.

757 Sime, L. C., Hindmarsh, R. C. A., and Corr, H.: Instruments and Methods Automated processing to derive dip angles of
758 englacial radar reflectors in ice sheets, *J. Glaciol.*, 57, 260–266, <https://doi.org/10.3189/002214311796405870>, 2011.

759 Sime, L. C., Karlsson, N. B., Paden, J. D., and Gogineni, S. P.: Isochronous information in a Greenland ice sheet radio echo
760 sounding data set, *Geophys. Res. Lett.*, 41, 1593–1599, <https://doi.org/10.1002/2013gl057928>, 2014.

761 Sullivan, C. and Kaszynski, A.: PyVista: 3D plotting and mesh analysis through a streamlined interface for the Visualization
762 Toolkit (VTK), *J. Open Source Softw.*, 4, 1450, <https://doi.org/10.21105/joss.01450>, 2019.

763 Sutter, J., Fischer, H., and Eisen, O.: Investigating the internal structure of the Antarctic ice sheet: the utility of isochrones for
764 spatiotemporal ice-sheet model calibration, *The Cryosphere*, 15, 3839–3860, <https://doi.org/10.5194/tc-15-3839-2021>,
765 2021.

766 Winter, A., Steinhage, D., Arnold, E. J., Blankenship, D. D., Cavitte, M. G. P., Corr, H. F. J., Paden, J. D., Urbini, S., Young,
767 D. A., and Eisen, O.: Comparison of measurements from different radio-echo sounding systems and synchronization with
768 the ice core at Dome C, Antarctica, *Cryosphere*, 11, 653–668, <https://doi.org/10.5194/tc-11-653-2017>, 2017.

769 Xiong, S., Muller, J.-P., and Carretero, R. C.: A New Method for Automatically Tracing Englacial Layers from MCoRDS
770 Data in NW Greenland, *Remote Sens.*, 10, 43, <https://doi.org/10.3390/rs10010043>, 2018.